J. Nanostruct Chem. 2026; 16(2): 151-171

Journal of Nanostructure in Chemistry (JNSC)

https://doi.org/10.57647/jnsc.2026.1602.08

Research Article

Cyclodextrin-Linked Corn Starch Nanostructured Microgels as pH-Responsive Nanocarriers for Doxorubicin Delivery in Hepatocellular Carcinoma

Shubin Wang[1], Teng Pan[2], Jiaqi Zhang[3], Hao Guo[3], Wuhan Yang[3,*]

[1]*Department of General Medicine, The Fourth Hospital of Hebei Medical University, Shijiazhuang, Hebei, 050000, China*
[2]*Department of Oncology, Shijiazhuang First Hospital, Shijiazhuang, Hebei, 050000, China*
[3]*Department of Hepatobiliary Surgery, The Fourth Hospital of Hebei Medical University, Shijiazhuang, Hebei, 050000, China*

*Corresponding authors: 18830671801@163.com; 48901882@hebmu.edu.cn

Article History:

Received:
09 December 2025

Revised:
04 January 2026

Accepted:
03 February 2026

Published in Issue:
30 April 2026

Abstract

Hepatocellular carcinoma chemotherapy remains constrained by off-target toxicity and multidrug resistance, underscoring the need for biobased nanostructured carriers capable of tumor microenvironment-responsive drug delivery. Here, we report cyclodextrin-linked corn starch nanostructured microgels prepared by inverse water-in-oil emulsion crosslinking with epichlorohydrin as a sustainable platform for doxorubicin delivery. Systematic variation of the β-cyclodextrin content generated colloidally stable microgels with hydrodynamic diameters in the 215–410 nm range, narrow polydispersity indices (~0.22–0.31) and increasingly negative zeta potentials down to −21.5 mV. Nitrogen sorption, FTIR, XRD and thermal analyses confirmed the formation of mesoporous polymer networks, with the lead formulation (CS-CD-3) exhibiting a BET surface area of 12.45 m²/g and an average pore diameter of 9.8 nm. Doxorubicin loading into these microgels afforded high drug payloads with an encapsulation efficiency of 78.4% for CS-CD-3. In vitro release studies demonstrated pronounced pH-dependent behavior, with only ~24% cumulative release at physiological pH 7.4 versus ~72% at pH 5.0 after 24 h, consistent with the intrinsic pH-dependent ionization of doxorubicin and the associated pH-modulated DOX–β-cyclodextrin host–guest interactions within the microgel network. Kinetic fitting of the pH 5.0 release data (Higuchi and Korsmeyer–Peppas models) indicated diffusion through a hydrated matrix with an additional polymer-relaxation contribution under acidic in vitro conditions ($n \approx 0.62$). Blank microgels preserved >90% cell viability in both HepG2 and L02 cells, whereas doxorubicin-loaded CS-CD-3 microgels decreased the IC50 in HepG2 cells from 2.15 ± 0.18 to 0.85 ± 0.12 μg/mL and increased the IC50 in L02 cells from 4.50 ± 0.35 to 8.20 ± 0.65 μg/mL, improving the selectivity index from 2.09 to 9.64. Confocal imaging confirmed efficient endocytic uptake, endo-lysosomal release and enhanced apoptotic nuclear damage. These results highlight nanostructured cyclodextrin–starch microgels as a promising bio-derived nanoplatform for safer, more selective hepatocellular carcinoma chemotherapy.

Keywords: Bio-based Polysaccharide Nanocarriers; β-cyclodextrin Crosslinked Microgels; Mesoporous Polymer Networks; Selective Cancer Chemotherapy Tumor; Microenvironment-responsive Release

Cite this article: Wang Sh., Pan T., Zhang J., Guo H., Yang W., Cyclodextrin-Linked Corn Starch Nanostructured Microgels as pH-Responsive Nanocarriers for Doxorubicin Delivery in Hepatocellular Carcinoma. *J Nanostruct Chem* **16**, 151-171 (2026). https://doi.org/10.57647/jnsc.2026.1602.08

1. Introduction

The global burden of hepatocellular carcinoma (HCC) continues to escalate, currently ranking as the sixth most prevalent neoplasm and the third leading cause of cancer-related mortality worldwide [1]. The etiology of HCC is multifactorial, strongly associated with chronic hepatitis B and C viral infections, alcohol-induced cirrhosis, and non-alcoholic steatohepatitis. Despite significant advancements in surveillance and diagnostic modalities, a substantial proportion of patients are diagnosed at intermediate or advanced stages where curative interventions such as surgical resection, radiofrequency ablation, or orthotopic liver transplantation are no longer viable options [2]. Consequently, systemic chemotherapy remains a cornerstone of palliative management. Among the pharmacological arsenal, Doxorubicin (DOX), an anthracycline antibiotic derived from *Streptomyces peucetius*, is widely utilized due to its potent efficacy in intercalating DNA base pairs and inhibiting topoisomerase II, thereby inducing apoptotic cell death in rapidly proliferating tumor cells [3].

However, the clinical utility of DOX in HCC is severely circumscribed by its non-selective distribution and narrow therapeutic index [4]. The systemic administration of free DOX is plagued by dose-limiting cardiotoxicity, myelosuppression, and the rapid development of multidrug resistance (MDR), mediated largely by the overexpression of ATP-binding cassette (ABC) transporters such as P-glycoprotein (P-gp) that actively efflux the drug from tumor cells [5]. Furthermore, the unique vascular architecture of the liver and the dense extracellular matrix in cirrhotic tissues pose significant barriers to effective drug penetration [6].

To circumvent these challenges, the development of intelligent, stimuli-responsive drug delivery systems (DDS) that can encapsulate chemotherapeutic agents, protect them from premature degradation, and facilitate targeted release within the tumor microenvironment (TME) has emerged as a paramount research frontier [7].

In recent years, polymeric microgels have garnered considerable attention as versatile carriers for anticancer therapeutics. Microgels are crosslinked, colloidal polymer networks that are swollen in a suitable solvent, combining the characteristics of macroscopic hydrogels with the advantages of micro- or nanoparticles, such as high specific surface area and tunable size [8].

Their porous structure allows for high drug loading capacities [9], while their soft, deformable nature facilitates extended circulation times and evasion of reticuloendothelial system (RES) clearance [10]. Among the plethora of polymers explored, polysaccharides are particularly attractive due to their inherent biocompatibility, biodegradability, abundance, and modifiability [11–13]. Within this class, starch offers a distinct set of practical and structural advantages for emulsion-templated microgel fabrication and drug-delivery translation.

First, starch (including maize/corn starch) is a long-established pharmaceutical/food ingredient with broad regulatory familiarity and mature industrial supply chains, which supports reproducibility and scale-up relative to more variable biologically sourced hydrocolloids.

Second, starch is densely functionalized with hydroxyl groups and can be efficiently converted into chemically robust hydrogel networks through ether-forming crosslinking reactions (e.g., epichlorohydrin), yielding matrices with enhanced resistance to pH and mechanical stresses compared with many physically ionically crosslinked gels.

Third, the amylose/amylopectin architecture enables tunable gelatinization and gel mechanics, allowing the aqueous precursor viscosity and network formation kinetics to be matched to water-in-oil droplet gelation and submicron particle formation. Consistent with this processing compatibility, epichlorohydrin-crosslinked starch particles have been successfully prepared via W/O emulsion routes with controllable size distributions.

Finally, starch derivatives such as hydroxyethyl starch have an established track record as doxorubicin carriers in stimuli-responsive anticancer systems, supporting the broader premise that starch-based backbones can be engineered into clinically relevant drug-delivery platforms. In contrast, for some alternative natural polymers (e.g., alginate), crude-source contaminants have been reported to provoke inflammatory responses unless rigorous purification is implemented, highlighting the translational value of compositionally well-defined polysaccharide feedstocks in biomedical carrier design.

Corn starch (CS), a natural biopolymer composed of linear amylose and branched amylopectin, represents an ideal candidate for constructing such microgels. It is non-toxic, renewable, and amenable to chemical crosslinking [14]. However, native starch granules exhibit poor mechanical stability in aqueous media and are susceptible to rapid enzymatic hydrolysis by α-amylase, limiting their use as sustained-release carriers [15]. Chemical modification via crosslinking with epichlorohydrin (ECH) creates ether linkages between hydroxyl groups of adjacent starch chains, forming a robust three-dimensional network that resists retrogradation and uncontrolled dissolution [16]. To further enhance the functionality of starch-based microgels, specifically their drug-loading efficiency and release control, the

incorporation of cyclodextrins (CDs) offers a synergistic strategy. CDs are cyclic oligosaccharides possessing a truncated cone shape with a hydrophilic exterior and a hydrophobic internal cavity [17].

This unique architecture enables CDs to form host-guest inclusion complexes with hydrophobic drug molecules like DOX, significantly improving their aqueous solubility and stability [18]. β-CDs (β-CD), comprising seven glucopyranose units, is particularly suitable for complexing anthracyclines due to the optimal size complementarity between its cavity and the drug's tetracyclic ring structure [19].

While starch microspheres and CD-based polymers have been investigated individually, the synthesis and extensive characterization of CD-linked polymer composite microgels derived from CS via inverse (W/O) emulsion crosslinking/gelation for HCC targeting remain insufficiently explored [20,21]. The rationale for this composite design is threefold: (1) The starch backbone provides a biodegradable, pH-responsive scaffold; (2) The covalently tethered β-CD moieties serve as high-affinity docking sites for DOX, minimizing premature leakage during circulation; and (3) The microgel architecture allows for passive targeting via the Enhanced Permeability and Retention (EPR) effect, characteristic of the hyperpermeable vasculature in solid tumors [22]. Crucially, the physiological differences between the tumor microenvironment (pH 6.5–6.8) and normal tissue (pH 7.4), along with the even more acidic environment of endosomes and lysosomes (pH 4.5–5.5), provide a basis for pH-triggered drug release [23]. We hypothesize that the CS-CD composite microgels will exhibit pH-dependent swelling and drug release profiles, facilitating intracellular DOX delivery upon endocytosis by hepatocytes. This research report presents a comprehensive study on the fabrication of CS-CD microgels using a surfactant-mediated water-in-oil (W/O) inverse emulsion technique. We systematically varied the mass ratio of β-CD to CS to elucidate the structure-property relationships governing particle morphology, crosslinking density, and drug encapsulation parameters. The synthesized microgels were subjected to extensive physicochemical characterization using Fourier Transform Infrared Spectroscopy (FTIR), X-ray Diffraction (XRD), Scanning and Transmission Electron Microscopy (SEM/TEM), X-ray Photoelectron Spectroscopy (XPS), and Brunauer-Emmett-Teller (BET) surface area analysis.

Furthermore, we evaluated the in vitro release kinetics under simulated physiological and tumor conditions, and assessed the cytotoxicity and cellular uptake in human hepatocellular carcinoma (HepG2) cells versus normal liver (L02) cells, providing robust evidence for their potential as a targeted therapeutic platform.

2. Materials and Methods

2.1. Materials and Reagents

CS with an amylose content of approximately 27% and moisture content <12% was purchased from Sigma-Aldrich (St. Louis, MO, USA). The starch was dried in a vacuum oven at 50 °C for 24 hours prior to use to ensure accurate weight measurements [24]. β-CDs (β-CD, purity >98%) was supplied by CycloLab (Budapest, Hungary) and was recrystallized twice from distilled water to remove any potential impurities or linear dextrins [25]. Epichlorohydrin (ECH, >99%), utilized as the crosslinking agent, and Sorbitan monooleate (Span 80), utilized as the lipophilic surfactant, were obtained from Sigma-Aldrich [26]. Doxorubicin hydrochloride (DOX·HCl, >98%) was purchased from Beijing Huafeng United Technology Co., Ltd. (Beijing, China).
The organic continuous phase solvent, cyclohexane (analytical grade), and other solvents such as acetone, ethanol, and sodium hydroxide (NaOH) were purchased from Sinopharm Chemical Reagent Co., Ltd. (Shanghai, China) and used without further purification. For biological assays, Dulbecco's Modified Eagle Medium (DMEM), fetal bovine serum (FBS), penicillin-streptomycin, trypsin-EDTA, and phosphate-buffered saline (PBS) were sourced from Gibco (Thermo Fisher Scientific, Waltham, MA, USA). 3-(4,5-dimethylthiazol-2-yl)-2,5-diphenyltetrazolium bromide (MTT) and 4',6-diamidino-2-phenylindole (DAPI) were obtained from Invitrogen. All aqueous solutions were prepared using double-distilled water (ddH_2O) with a resistivity >18.2 MΩ· cm.

2.2. Synthesis of CS-CD Polymer Composite Microgels

The synthesis of the β-CD-linked CS microgels was executed via a carefully controlled inverse (W/O) emulsion crosslinking (inverse emulsification/gelation) technique. In this approach, the dispersed aqueous droplets serve as confined microreactors in which epichlorohydrin forms ether crosslinks between starch and β-cyclodextrin hydroxyls, yielding discrete, solvent-swellable gel particles (microgels/nanogels) upon purification [26]. Initially, varying amounts of CS (0.5 g to 2.0 g) were dispersed in 20 mL of 1.5 N NaOH aqueous solution. The mixture was mechanically stirred at 60 °C for 45 minutes to facilitate the gelatinization of starch, disrupting the granular semi-crystalline structure and exposing the hydroxyl groups.20 Subsequently, calculated quantities of β-CD were added to the gelatinized starch paste. The mixture was stirred for an additional 30 minutes until a homogeneous, translucent solution was obtained. The specific feed compositions for

10.57647/jnsc.2026.1602.08

the five distinct formulations (CS-CD-0 to CS-CD-4) are detailed in Table 1.

The organic phase was prepared by dissolving Span 80 (4% v/v) in 150 mL of cyclohexane in a three-neck round-bottom flask equipped with a mechanical stirrer, a reflux condenser, and a nitrogen inlet. The aqueous starch/β-CD solution was added dropwise to the organic phase under vigorous stirring at 1200 rpm at room temperature. The system was purged with nitrogen gas for 30 minutes to remove dissolved oxygen. The high shear rate and the surfactant facilitated the formation of a stable water-in-oil (W/O) emulsion containing starch/β-CD droplets.

Once the emulsion was stabilized, the temperature was raised to 60 °C. The crosslinker, ECH (1.0 mL), was introduced dropwise into the reaction vessel over a period of 15 minutes. The polymerization/crosslinking reaction was allowed to proceed for 6 hours under continuous stirring at 60 °C. During this phase, ECH reacts with the hydroxyl groups of both starch and β-CD under alkaline catalysis, forming stable ether linkages and creating a three-dimensional polymer network within the aqueous droplets.

Upon completion, the reaction mixture was cooled to room temperature. The microgels were precipitated by the addition of excess acetone, which breaks the emulsion. The precipitate was collected via suction filtration and subjected to a rigorous washing protocol: first with cyclohexane to remove residual Span 80, followed by ethanol to remove unreacted ECH, and finally with copious amounts of distilled water to remove NaOH and any unreacted carbohydrates.

The purified microgels were dialyzed (MWCO 12,000 Da) against distilled water for 24 hours to ensure high purity. Finally, the products were lyophilized (freeze-dried) at -50 °C for 48 hours to obtain the final white, porous microgel powders.

2.3. Swelling Studies

The swelling behavior of the microgels was investigated gravimetrically in buffer solutions with different pH values (1.2, 5.0, 6.8, and 7.4). A known weight of dry microgels ($W_d \approx 50$ mg) was enclosed in a pre-weighed tea bag (nylon mesh) and immersed in 50 mL of the respective buffer at 37 °C. At predetermined time intervals, the bags were removed, gently blotted with filter paper to remove excess surface water, and weighed (W_s). The swelling equilibrium was monitored until a constant weight was achieved. The equilibrium swelling ratio (ESR) was calculated using the following equation:

$$ESR(\%)=\frac{W_s-W_d}{W_d}\times 100$$

where W_s is the weight of the swollen hydrogel and W_d is the weight of the dry hydrogel.

2.4. Drug Loading and Encapsulation

Doxorubicin (DOX) loading was achieved via the swelling–diffusion method. Briefly, 100 mg of dry microgels were dispersed in 20 mL of DOX aqueous solution (1.0 mg/mL) and stirred at room temperature for 24 h in the dark to prevent drug photodegradation. The pH of the loading solution was adjusted to 8.0 to shift DOX toward a less protonated, more hydrophobic form (pKa ~8.2), which favors partitioning into hydrophobic domains and host–guest association with β-cyclodextrin cavities.

To directly validate the inclusion mechanism at the molecular level, 2D NMR (NOESY/ROESY) is most informative because it can reveal through-space correlations between β-CD cavity protons (H-3/H-5) and aromatic protons of DOX; however, because the final CS-CD microgels are crosslinked and not suitable for high-resolution solution NMR, such 2D experiments are best implemented using a soluble model system (e.g., DOX with β-CD or with the soluble CS-CD fraction/precursor) to confirm the characteristic host–guest contacts [27]. After loading, the suspension was centrifuged at 12,000 rpm for 15 minutes.

The supernatant was collected, and the concentration of free DOX was determined using a UV–vis spectrophotometer (Shimadzu UV-2600) at λ_max = 480 nm. For spectral characterization, full UV–vis absorption spectra were recorded over 350–650 nm using matched quartz cuvettes, with baseline subtraction using the corresponding DOX-free buffer as reference.

To provide a direct reference for the release-study pH conditions, pH-dependent DOX spectra were additionally measured by preparing DOX solutions at the same concentration in PBS (pH 7.4) and acetate buffer (pH 5.0), followed by immediate spectral acquisition under identical instrument settings. The Drug Loading Content (DLC) and Encapsulation Efficiency (EE) were calculated as follows [28]:

$$DLC\ (\%)=\frac{M_{total}-M_{free}}{M_{microgels}}\times 100$$

$$EE\ (\%)=\frac{M_{total}-M_{free}}{M_{total}}\times 100$$

where M_{total} is the total mass of DOX initially added, M_{free} is the mass of free DOX in the supernatant, and $M_{microgels}$ is the mass of the polymer carrier.

2.5. In Vitro Drug Release

The in vitro release profile of DOX from the microgels was evaluated using the dialysis bag diffusion technique. The drug-loaded microgels (equivalent to 2 mg of DOX) were resuspended in 2 mL of release medium and placed

10.57647/jnsc.2026.1602.08

into a dialysis bag (MWCO 3.5 kDa). The bag was immersed in 50 mL of release medium (PBS at pH 7.4 or Acetate buffer at pH 5.0) and incubated at 37 °C with constant shaking at 100 rpm. At scheduled time points (0.5, 1, 2, 4, 6, 8, 12, 24, 36, 48 h), 3 mL of the release medium was withdrawn and replaced with an equal volume of fresh medium to maintain sink conditions. The DOX content was analyzed spectrophotometrically.

The cumulative release percentage (Q_n) was calculated using the equation:

$$Q_n(\%)=\frac{V_0C_n+V\sum_{i=1}^{n-1}C_i}{M_{drug}}\times 100$$

where V_0 is the total volume of release medium, V is the sampling volume, C_n is the drug concentration at time point n, and M_{drug} is the total mass of encapsulated drug.

2.6. Cell Culture and In Vitro Cytotoxicity

Human hepatocellular carcinoma (HepG2) and human normal liver (L02) cell lines were cultured in DMEM supplemented with 10% FBS and 1% penicillin-streptomycin at 37 °C in a humidified atmosphere containing 5% CO_2. The cytotoxicity of the free DOX, blank microgels, and DOX-loaded microgels was assessed using the MTT assay. Cells were seeded in 96-well plates at a density of 5×10^3 cells/well and allowed to attach for 24 hours.

The medium was then replaced with fresh medium containing serial dilutions of the test samples. After 24 or 48 hours of incubation, 20 µL of MTT solution (5 mg/mL) was added to each well and incubated for another 4 hours. The formazan crystals formed were dissolved in 150 µL of DMSO, and the absorbance was measured at 570 nm using a microplate reader (Bio-Rad). Cell viability was expressed as a percentage of the control (untreated cells) [29].

2.7. Cellular Uptake Studies

To visualize the cellular uptake and intracellular distribution of DOX, HepG2 cells were seeded on sterile glass coverslips in 6-well plates (1×10^5 cells/well). After 24 hours, the cells were treated with free DOX or DOX-loaded microgels (equivalent DOX concentration of 5 µg/mL) for 2 and 4 hours. Subsequently, the cells were washed with PBS, fixed with 4% paraformaldehyde for 15 minutes, and the nuclei were stained with DAPI (1 µg/mL) for 10 minutes. The coverslips were mounted on glass slides, and fluorescence images were acquired using a Leica TCS SP8 confocal laser scanning microscope (CLSM). The excitation wavelengths were set at 405 nm for DAPI (blue emission) and 488 nm for DOX (red emission) [30].

3. Results and Discussion

3.1. Synthesis and Optimization of Composite Microgels

The synthesis of the CS-CD microgels was based on the covalent crosslinking of CS and β-CD within the aqueous droplets of a W/O inverse emulsion. The surfactant Span 80 (HLB 4.3) was selected for its efficacy in stabilizing aqueous droplets in cyclohexane [31]. Because crosslinking proceeds *within each droplet* to form a covalent three-dimensional network, the product is a population of discrete hydrogel particles. Their classification as microgels/nanogels is further supported by the large equilibrium swelling ratios and reversible swelling–deswelling behavior, which are defining functional attributes of gel particles and distinguish them from rigid solid nanoparticles produced by precipitation or crystallization routes. ECH was chosen as the crosslinker due to its ability to form stable glycerol diether bonds, which are resistant to hydrolysis in physiological conditions compared to ester bonds, thereby ensuring the structural integrity of the microgels during systemic circulation [32]. Optimization of the synthesis parameters revealed that the ratio of the aqueous phase to the organic phase and the stirring speed were critical determinants of particle size [33]. A stirring speed of 1200 rpm was found to yield microgels in the sub-micron range (200–500 nm). Lower speeds resulted in millimeter-sized beads, while higher speeds caused emulsion instability. Five formulations were prepared by varying the mass ratio of CS to β-CD, as detailed in Table 1. The yield of the reaction remained consistently high (>80%), indicating efficient incorporation of the reactants into the crosslinked network.

Table 1. Composition and physical properties of synthesized CS-CD microgels

Sample Code	Starch (g)	β-CD (g)	ECH (mL)	Yield (%)	Size (Dh, nm)[a]	PDI[a]	Zeta Potential (mV)[b]
CS-CD-0	2.0	0	1.0	82.5	215 ± 12	0.22	-12.4 ± 1.5
CS-CD-1	1.8	0.2	1.0	84.1	245 ± 15	0.25	-15.8 ± 2.1
CS-CD-2	1.5	0.5	1.0	86.3	298 ± 18	0.28	-18.2 ± 1.8
CS-CD-3	1.0	1.0	1.0	88.0	345 ± 22	0.29	-21.5 ± 2.4
CS-CD-4	0.5	1.5	1.0	85.7	410 ± 25	0.31	-24.1 ± 1.9

Notes: [a] Measured by DLS in PBS (pH 7.4). [b] Measured at pH 7.0

10.57647/jnsc.2026.1602.08

As the β-CD feed increased from 0 to 1.5 g (CS-CD-0 → CS-CD-4), the hydrodynamic diameter (Dh) increased monotonically from 215 ± 12 nm to 410 ± 25 nm (Table 1). Because the total polysaccharide mass was held constant (2.0 g in all formulations) while the ECH dose was fixed (1.0 mL), this trend is best interpreted as a formulation-driven change in network architecture rather than a simple solids-loading effect. Two coupled factors act in the same direction. First, increasing the β-CD fraction introduces bulky cyclic units that enlarge the effective segmental steric volume of the chains and can increase the hydrodynamic drag of the solvated particle, which is widely observed when cyclodextrins are grafted/introduced into polymeric nanostructures. Second, under a fixed crosslinker dose, adding β-CD increases the total number of available hydroxyl functionalities competing for ECH, thereby reducing the effective crosslinking density per repeat unit (lower crosslinker-to-functional-group ratio). A lower crosslink density is expected to yield a looser gel mesh, higher water uptake, and therefore a larger Dh in aqueous media—an established structure–property relationship in hydrogel/microgel systems. In addition, inverse W/O emulsion crosslinking of starch with epichlorohydrin is known to be sensitive to network formation and droplet solidification kinetics, and compositional changes that alter crosslinking efficiency can translate into systematic particle-size shifts even at constant stirring conditions [34]. The zeta potential values were consistently negative, ranging from -12.4 mV to -24.1 mV. While starch and β-CD are nominally neutral polysaccharides, the alkaline condition during synthesis (1.5 N NaOH) can induce partial oxidation of the hydroxyl groups to carboxylate groups ($-COO^-$), conferring a negative charge [35]. Furthermore, it has been reported that ECH crosslinking can trap residual ionic species or induce minor side reactions that contribute to surface charge. The increasing magnitude of the negative potential with higher β-CD content suggests that the modified β-CD-rich network may be more susceptible to such alkaline modifications or that the specific conformation of β-CD exposes more electronegative domains at the shear plane [36,37]. This negative surface charge is highly advantageous for colloidal stability (preventing aggregation via electrostatic repulsion) and for biological applications, as highly positive particles are often associated with greater cytotoxicity and opsonization [38].

3.2. Structural Characterization via FTIR

Fig. 1 presents the FTIR spectra of native CS, pure β-CD, and the representative composite microgel formulation CS-CD-3, providing direct spectroscopic evidence for successful epichlorohydrin (ECH) crosslinking and chemical integration of β-CD within the starch backbone. Native starch exhibits the typical fingerprint of a polysaccharide: a broad and intense O–H stretching band centered around 3410 cm^{-1} arising from extensive intra- and intermolecular hydrogen bonding, a C–H stretching band near 2930 cm^{-1} attributed to aliphatic C–H vibrations of the glucopyranose rings, and a series of characteristic C–O–C and C–O vibrations between 1156 and 1015 cm^{-1} associated with the glycosidic linkages and secondary hydroxyl groups. In the β-CD spectrum, these general features of carbohydrate structures are retained but appear as sharper, more defined bands, reflecting its higher crystallinity and ordered cage-like packing. In particular, the band near 1025 cm^{-1}, commonly assigned to α-1,4-glycosidic stretching in β-CD, and the peak around 940 cm^{-1}, associated with skeletal vibrations of the glucopyranose ring, are more prominent, consistent with the well-organized lattice of β-CD crystals. The spectrum of CS-CD-3 shows several distinct changes relative to both precursors, which collectively confirm that a new crosslinked, composite network has been formed rather than a simple physical mixture [39]. First, the broad O–H stretching envelope undergoes a slight shift to lower wavenumber (ca. 3380 cm^{-1}) and noticeable broadening. This shift indicates strengthening and reorganization of the hydrogen-bonding network due to the introduction of ECH-derived ether bridges and the covalent tethering of β-CD rings. The broader profile suggests a more heterogeneous distribution of hydrogen-bonding environments, as would be expected in an amorphous, chemically crosslinked hydrogel matrix in which hydroxyl groups are involved in both intra-chain and inter-chain interactions, as well as in interactions with newly introduced ether oxygen atoms.

A second, and more definitive, feature of the CS-CD-3 spectrum is the appearance of a shoulder around 1260 cm^{-1} together with an increase in intensity across the 1050–1100 cm^{-1} region. These bands are characteristic of C–O–C asymmetric stretching in aliphatic ether linkages. Their enhancement in CS-CD-3, compared with native starch and β-CD, is consistent with the formation of glycerol-type diether bridges resulting from the nucleophilic attack of deprotonated hydroxyl groups on the epoxide ring of ECH during crosslinking [40]. The intensified ether-related bands thus provide a molecular-level signature of the three-dimensional poly(ether) network that stabilizes the microgel architecture in aqueous media and under physiological conditions [41]. Concomitantly, the C–H stretching band near 2925 cm^{-1} becomes relatively more intense in CS-CD-3, reflecting the contribution of additional methylene groups introduced via the ECH spacer. Equally important is the absence in the CS-CD-3 spectrum of any residual band around 910 cm^{-1}, which would correspond to the epoxide ring vibration of unreacted ECH. The complete disappearance of this feature indicates that the vast

10.57647/jnsc.2026.1602.08

majority of epoxide groups have reacted during synthesis or have been efficiently removed during the subsequent washing and dialysis steps. This observation not only supports the chemical completeness of the crosslinking reaction but also has safety implications, as residual ECH is known to be cytotoxic and genotoxic [42]. The lack of a detectable epoxide signal therefore corroborates the suitability of the purified microgels for biomedical applications. It is also noteworthy that the spectral features associated with the ordered crystalline structures of both native starch and β-CD are significantly attenuated or overlapped in CS-CD-3. In particular, the sharper β-CD bands at 1025 and 940 cm^{-1} lose their distinct definition, merging into a broader, less structured envelope characteristic of an amorphous polymer network [43]. Combined with the broad, featureless baseline in the fingerprint region, this behavior implies that covalent linking of β-CD to gelatinized starch chains prevents the re-formation of the native crystalline packing of either component [44]. This interpretation is fully consistent with the XRD data showing the disappearance of sharp Bragg peaks and the appearance of a broad halo in the CS-CD-3 diffractogram [45]. The transition from crystalline to amorphous organization is advantageous for drug delivery, as amorphous matrices generally exhibit higher free volume, enhanced water accessibility, and improved swelling behavior, all of which contribute to increased drug loading capacity and more tunable release kinetics [46].From a functional perspective, the FTIR signatures observed in Figure 1 underpin several key performance attributes of the microgels. The strengthened and diversified hydrogen-bond network, evident from the broadened O–H band, is directly related to the high-water uptake and pronounced pH-responsive swelling behavior reported for CS-CD-3. The dense population of ether linkages indicated by the 1260 and 1050–1100 cm^{-1} bands confers improved thermal and hydrolytic stability, as the C–O–C bonds formed from ECH are resistant to cleavage under neutral and mildly acidic conditions compared with ester bonds. This structural robustness is essential to prevent premature disintegration of the carriers in circulation while still permitting controlled swelling and erosion in the acidic tumor or endosomal microenvironment. Finally, the implicit presence of chemically bound β-CD, although not represented by a single diagnostic peak, is reflected in the composite nature of the polysaccharide backbone and provides the molecular basis for high-affinity host–guest complexation with doxorubicin. The hydrophobic internal cavity of β-CD, anchored within a hydrophilic, crosslinked starch framework, creates a heterogeneous microenvironment capable of simultaneously accommodating DOX via inclusion complex formation and regulating its diffusion through the hydrated polymer mesh.

3.3. Crystallinity Analysis via XRD

Fig. 2 provides direct crystallographic evidence that the β-CD-linked corn starch microgels have undergone a profound structural reorganization from a semi-crystalline polysaccharide system and a highly crystalline oligosaccharide host into a predominantly amorphous polymer network. Native corn starch exhibits the expected A-type pattern, with intense reflections at $2\theta \approx 15°$, 17°, 18°, and 23°, arising from the ordered double-helical packing of amylopectin side chains within the granule. These sharp Bragg peaks testify to a relatively high degree of long-range order and a compact packing mode, which inherently limits free volume and water accessibility inside the matrix. In parallel, β-CD displays a different but equally well-defined diffraction fingerprint, with numerous narrow peaks in the low- and mid-angle region that reflect its cage-like crystalline lattice. The coexistence of these highly ordered structures in the precursors would, in principle, be detrimental for drug delivery, because crystalline domains typically show low swelling capacity and restricted diffusional pathways for guest molecules such as doxorubicin.

Upon gelatinization of starch and subsequent epichlorohydrin (ECH) crosslinking in the presence of β-CD, the situation is dramatically altered. The diffractogram of CS-CD-3 is dominated by a broad, featureless halo centered around $2\theta \approx 20°$, with the complete disappearance of the characteristic starch and β-CD reflections. This loss of discrete Bragg peaks indicates that the regular packing of both macromolecular components has been effectively destroyed and replaced by an amorphous poly(ether) network in which starch chains and β-CD units are randomly crosslinked rather than re-assembled into their native lattices. The gelatinization step disrupts the granular crystallites, while covalent tethering of β-CD to the solubilized starch chains prevents recrystallization during drying. The amorphization inferred from Figure 2 is consistent with the FTIR evidence of extensive ether bond formation and hydrogen-bond reorganization, and with the increased BET surface area and mesoporosity measured for CS-CD-3. From a functional standpoint, this structural transformation is highly advantageous: amorphous matrices generally possess higher free volume, enhanced water uptake, and more flexible chain segments, all of which facilitate rapid swelling, efficient diffusion of DOX into and out of the microgels, and pH-responsive relaxation of the network. Thus, the XRD pattern in Figure 2 not only confirms successful ECH-mediated crosslinking and β-CD integration at the molecular level, but also underpins the superior loading capacity and tunable release behavior that are critical for the intended targeted chemotherapy of hepatocellular carcinoma.

10.57647/jnsc.2026.1602.08

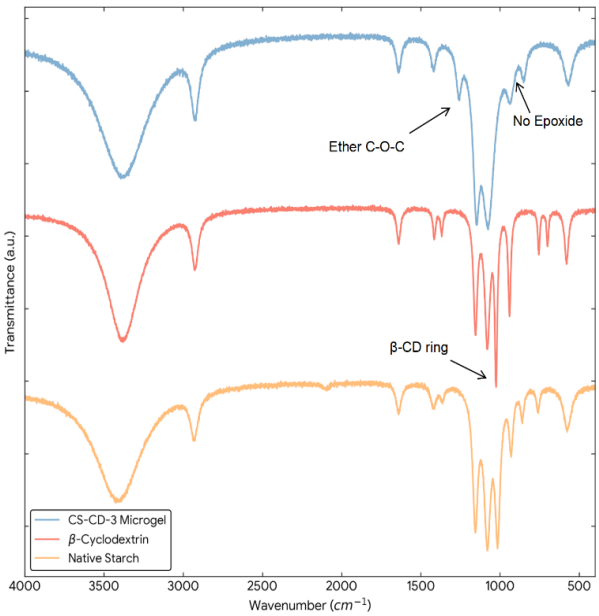

Figure 1. FTIR spectra of native CS, pure β-CD, and the CS-CD-3 composite microgels

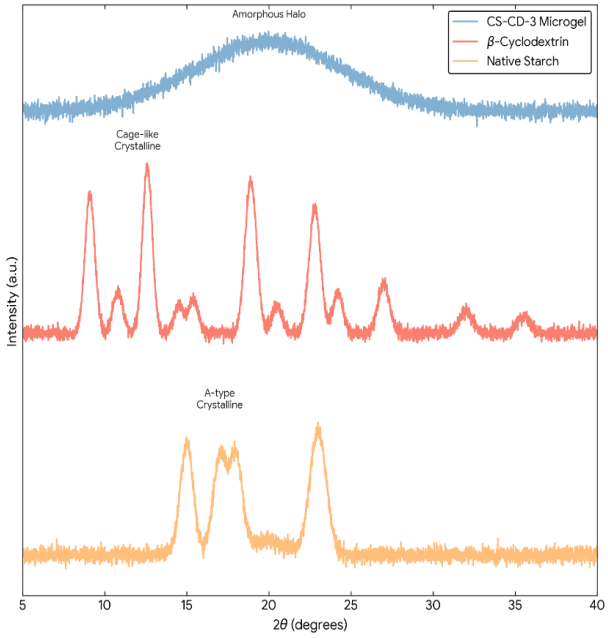

Figure 2. XRD patterns of native CS, β-CD, and CS-CD-3 composite microgels in the 2θ range of 5–40°

3.4. Morphological Evaluation

The combined information from Figures 3–5 provides a coherent picture of how β-CD incorporation modulates the morphology and colloidal characteristics of the corn starch–based microgels and how these features underpin their performance as drug delivery vehicles. SEM images in Fig. 3 confirm that the inverse emulsion crosslinking strategy reliably produces spherical particles across all formulations, with mean diameters that increase systematically as the β-CD content is raised from 0 to 1.5 g. The starch-only microgels (CS-CD-0) appear as relatively smooth, compact spheres with limited surface texturing, indicative of a dense crosslinked starch network. In contrast, the composite microgels containing equimass starch and β-CD (CS-CD-3) display slightly larger diameters and a noticeably rougher, more corrugated surface, which becomes even more pronounced in the highly β-CD-rich CS-CD-4 sample where some interparticle bridging and aggregation can be observed. This evolution in surface morphology is consistent with the introduction of bulky β-CD rings and the concomitant reduction in effective crosslinking density per unit polymer mass when the total number of hydroxyl groups is increased at a fixed epichlorohydrin level. The rough, wrinkled surfaces of β-CD-rich particles likely reflect microphase separation or local heterogeneity in crosslink density during solvent removal, and they are expected to contribute beneficially to the accessible surface area and interfacial area for drug adsorption and diffusion [47]. TEM analysis of CS-CD-3 in Fig. 4 further refines this picture at the nanoscale. The low-magnification view confirms that the particles remain well-dispersed and maintain their spherical morphology in the fully hydrated and then dried state, indicating that the crosslinked network is mechanically robust enough to withstand the stresses associated with sample preparation. At higher magnification, individual microgels exhibit a relatively homogeneous internal electron density with slightly less dense peripheral regions, a typical signature of soft, gel-like polymer networks that have experienced partial collapse upon drying [48]. Critically, no sharp interfaces, layered domains, or lattice fringes associated with crystalline structures are detected, supporting the XRD evidence that both the native A-type starch crystallinity and the cage-like β-CD lattice have been effectively disrupted during gelatinization and crosslinking, giving rise to an amorphous poly(ether) network. This amorphous, sponge-like internal architecture is advantageous for drug delivery because it provides enhanced free volume and continuous diffusion pathways for Doxorubicin molecules to penetrate the microgel interior and subsequently diffuse out under stimulus conditions. The DLS histograms in Fig. 5 quantitatively corroborate the size trends inferred from microscopy and provide essential information on the hydrodynamic behavior of the microgels in aqueous environments relevant to biological use. For both CS-CD-0 and CS-CD-3, the particle size distributions are unimodal with PDI values below 0.30, indicating relatively narrow size dispersity and the absence of significant aggregation or large secondary structures in PBS. The increase in mean hydrodynamic diameter from ~215 nm for CS-CD-0 to ~345 nm for CS-CD-3 mirrors the composition-dependent size increase observed by SEM, though the DLS values are slightly larger due to hydration and extended polymer chains at the particle–solvent interface [49]. Importantly, the 200–400 nm size

10.57647/jnsc.2026.1602.08

window achieved for the optimized CS-CD-3 formulation falls squarely within the range generally considered favorable for enhanced permeability and retention (EPR)–mediated accumulation in solid tumors, while remaining small enough to avoid rapid clearance by the spleen and liver sinusoids. When combined with the moderately negative zeta potential reported in Table 1, these data suggest that CS-CD-3 microgels should maintain good colloidal stability in physiological media and exhibit reduced nonspecific interactions with serum proteins and cell membranes compared with strongly cationic carriers.

3.5. Porosity and BET Surface Area

Fig. 6 illustrates how inverse-emulsion crosslinking and β-CD integration fundamentally alter the textural properties of corn starch, transforming a nearly non-porous biopolymer into a mesoporous carrier suitable for chemotherapeutic loading. Native starch shows only a modest nitrogen uptake over the full relative pressure range, with no pronounced hysteresis, consistent with its very low BET surface area (0.56 ± 0.05 m^2/g) and negligible pore volume (0.002 cm^3/g) reported in Table 2. For CS-CD-3, the isotherm evolves into a type IV profile with an H3 hysteresis loop at high P/P_0, which is characteristic of capillary condensation in mesopores and slit-like pore geometries according to IUPAC classification. In contrast, the crosslinked starch-only microgels (CS-CD-0) already display enhanced adsorption, reflecting the generation of intra- and interparticle voids during epichlorohydrin crosslinking; this is corroborated by an increase in surface area to 4.23 ± 0.12 m^2/g and a pore volume of 0.015 cm^3/g, with an average pore diameter of 15.4 nm. The most striking change is observed for CS-CD-3, whose isotherm evolves into a clear type IV profile with a well-defined H3 hysteresis loop at high P/P_0, a hallmark of mesoporous systems with slit-like or wedge-shaped pores [50]. This textural state is quantified by a roughly threefold increase in surface area over CS-CD-0 to 12.45 ± 0.25 m^2/g and a pore volume of 0.048 cm^3/g, while the mean pore diameter narrows into the mesoporous regime at 9.8 nm. Quantitatively, CS-CD-3 shows an increased surface area (12.45 ± 0.25 m^2/g) and pore volume (0.048 cm^3/g), and the mean pore diameter (9.8 nm) falls within the mesoporous size range (2–50 nm). While the absolute BET surface area (~12 m^2/g) is modest compared with highly porous inorganic mesostructures or aerogels, it represents a substantial enhancement relative to native starch and is consistent with the development of mesopore-range void space within this crosslinked polysaccharide microgel platform.

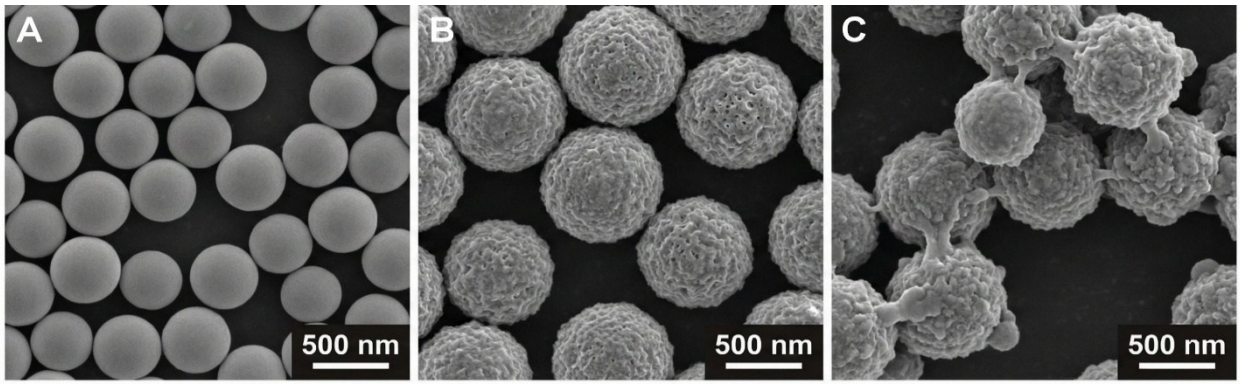

Figure 3. SEM micrographs of lyophilized CS-CD microgels prepared with different β-CD contents: (A) CS-CD-0 (starch-only control, 0 g β-CD); (B) CS-CD-3 (1.0 g starch / 1.0 g β-CD); and (C) CS-CD-4 (0.5 g starch / 1.5 g β-CD)

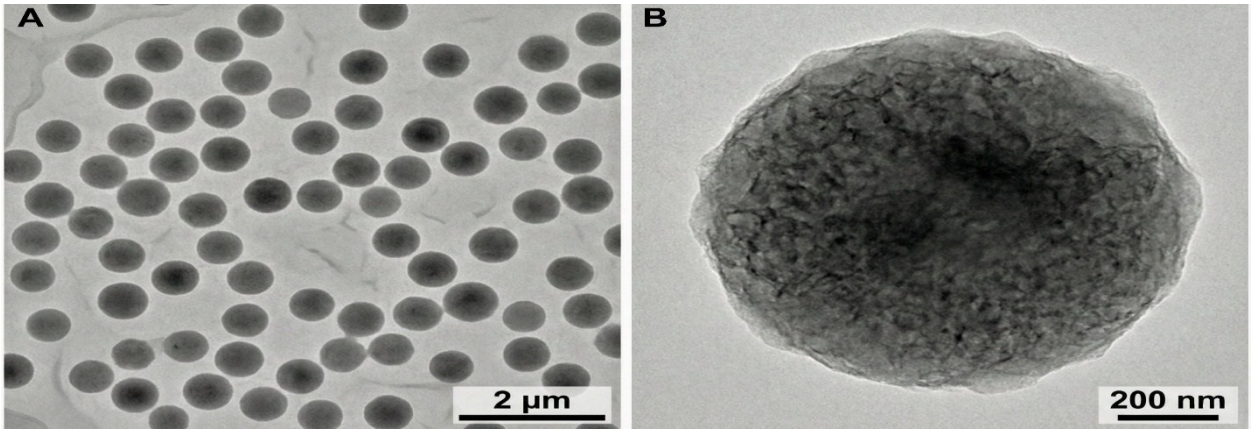

Figure 4. TEM images of CS-CD-3 composite microgels. (A) Low-magnification view showing a uniform population of well-dispersed, nearly spherical microgels. (B) High-magnification image of a representative single particle

10.57647/jnsc.2026.1602.08

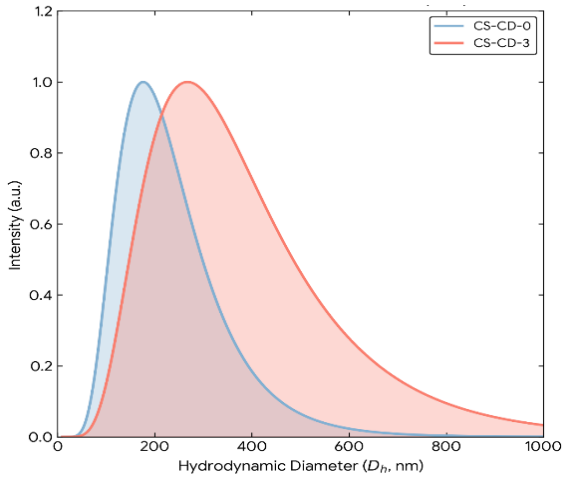

Figure 5. Particle size distribution histograms of CS-CD-0 and CS-CD-3 microgels measured by DLS in PBS (pH 7.4)

Table 2. Textural Properties and Thermal Analysis

Sample	BET Surface Area (m^2/g)	Pore Volume (cm^3/g)	Avg. Pore Diameter (nm)	Tmax (°C)[c]
Native Starch	0.56 ± 0.05	0.002	-	312
CS-CD-0	4.23 ± 0.12	0.015	15.4	335
CS-CD-3	12.45 ± 0.25	0.048	9.8	358

Notes: [c] Temperature of maximum decomposition rate from DTG

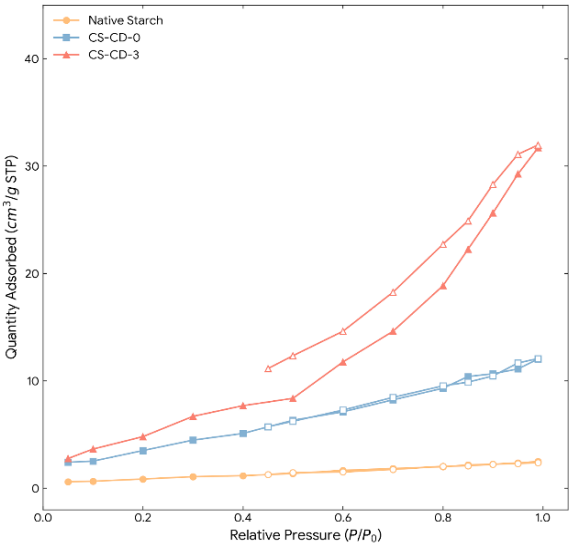

Figure 6. N_2 adsorption–desorption isotherms of native corn starch, CS-CD-0 microgels, and β- CD-containing CS-CD-3 composite microgels

The combination of increased BET surface area, pore volume, and mesopore-range voids in the dry state is expected to influence Doxorubicin loading by increasing interfacial contact and providing additional accessible pathways within the matrix [51]. At the same time, we emphasize that N_2 sorption/BET primarily probes nitrogen-accessible surfaces after drying, whereas CS-CD microgels function as soft, highly hydrated networks in aqueous media; therefore, the magnitude of BET surface area should not be interpreted as a direct measure of the swollen-state free volume or transport pathways. Consistent with this distinction, polysaccharide aerogels produced by drying routes that better preserve the pore network can exhibit surface areas on the order of ~200 m^2/g, whereas starch-derived porous hydrogels/cryogels that experience partial pore collapse upon drying often show much lower BET values despite retaining functional water uptake and diffusion in the hydrated state. Low-to-moderate BET areas in the single-digit to low–tens m^2/g range are also commonly reported for crosslinked polymeric hydrogel materials where porosity exists but is not fully accessible to N_2 in the dry state.

First, the larger accessible surface and network of mesopores provide abundant interfaces and diffusion pathways for DOX molecules (hydrodynamic size ~1.5 nm) to penetrate deep into the microgel matrix rather than being confined to the outer shell, which helps explain the marked increase in encapsulation efficiency from 22.5% for starch-only carriers to 78.4% for CS-CD-3. Second, the slit-shaped mesopores associated with H3 hysteresis are typically formed by loosely packed plate-like or lamellar domains; in this system, they likely originate from β-CD-rich regions and amorphous starch segments that pack inefficiently, leaving interstitial voids. Under neutral conditions, these mesopores and the hydrophobic β-CD cavities cooperatively trap DOX, supporting the slow, diffusion-limited release observed at pH 7.4. Under mildly acidic conditions, protonation of DOX and partial relaxation of the hydrated network facilitate its desorption from the β-CD cavities and migration through these mesoporous channels, giving rise to accelerated release at pH 5.0. Thus, Figure 6 not only confirms that CS-CD-3 possesses a well-developed mesoporous structure but also provides a structural basis for the high drug-loading capacity and pH-responsive release behavior that underpin the therapeutic performance of the microgels [52].

3.4. Thermal Stability (TGA/DSC)

The thermal analysis summarized in Fig. 7 clearly demonstrates that inverse-emulsion crosslinking and β-CD integration substantially enhance the thermal stability of corn starch–based carriers. Native starch exhibits the typical two-step mass-loss behavior of polysaccharides: an initial weight loss of approximately 10% below 100 °C, attributed to the evaporation of physically adsorbed and weakly bound water, followed by a sharp, single main degradation event starting at around 290 °C and peaking at $T_{max} \approx 312$ °C, which corresponds to depolymerization, glycosidic bond cleavage, and the formation of volatile decomposition products. The relatively low T_{max} and

10.57647/jnsc.2026.1602.08

modest char residue (~12.5% at 600 °C) reflect the limited structural integrity of the uncrosslinked starch matrix.

In contrast, both CS-CD-0 and CS-CD-3 display a distinctly different thermal response. The crosslinked starch-only microgels already show a slight increase in low-temperature mass loss, indicative of higher hydrophilicity and water-holding capacity, but more importantly, their main degradation step is shifted to higher temperatures, with T_{max} increasing to about 335 °C. This shift signifies that the epichlorohydrin-derived poly(ether) network constrains chain mobility and requires more energy to disrupt, thereby delaying backbone scission. The introduction of β-CD in CS-CD-3 further amplifies this effect: the onset of major decomposition is postponed to around 320 °C and T_{max} is elevated to 358 °C, giving a total increment of 46 °C relative to native starch. Such a pronounced increase in T_{max} is a strong signature of successful covalent crosslinking and the formation of a denser, more cohesive three-dimensional network [53]. The trends observed in the TGA curves are mirrored by the DTG profiles and by the residual char content. CS-CD-3 not only decomposes at higher temperatures but also leaves a significantly larger char yield (24.6% at 600 °C) compared with native starch [54]. This higher residue suggests a greater proportion of thermally robust structures, such as ECH-derived ether bridges and condensed carbonaceous domains formed from the β-CD-rich network during pyrolysis. The intermediate behavior of CS-CD-0 in both T_{max} and char yield confirms that β-CD contributes cooperatively with starch to building a more thermally resistant architecture.

3.5. Swelling Behavior and pH Responsiveness

The swelling data presented in Figs. 8 and 9 highlight the pronounced pH-responsiveness and mechanical robustness of the CS-CD-3 composite microgels, which are central to their performance as doxorubicin delivery carriers for hepatocellular carcinoma. As shown in Fig. 8, CS-CD-3 particles exhibit rapid water uptake in all tested media, with the ESR approaching a plateau within roughly 4 h, indicating that the hydrogel network can reorganize and equilibrate on a time scale compatible with in vivo residence times. The equilibrium degree of swelling is strongly dependent on pH. At pH 7.4, which mimics the physiological environment of blood and normal tissue, the microgels display the highest expansion, with an ESR on the order of ~1850%. This extensive volume increase is attributed to deprotonation of carboxylic groups introduced during alkaline processing and partial oxidation of the polysaccharide backbone; the resulting fixed negative charges generate strong electrostatic repulsion along the polymer chains, increase the osmotic pressure of mobile counterions inside the network, and drive maximum chain extension and water uptake. When the pH is lowered to 5.0, representative of the mildly acidic tumor milieu and endosomal compartments, the equilibrium swelling remains substantial but decreases to about ~1400%. In this regime, a fraction of the ionizable groups is protonated, partially screening electrostatic repulsion and allowing closer chain packing, while the network still retains enough charge to maintain a swollen state.

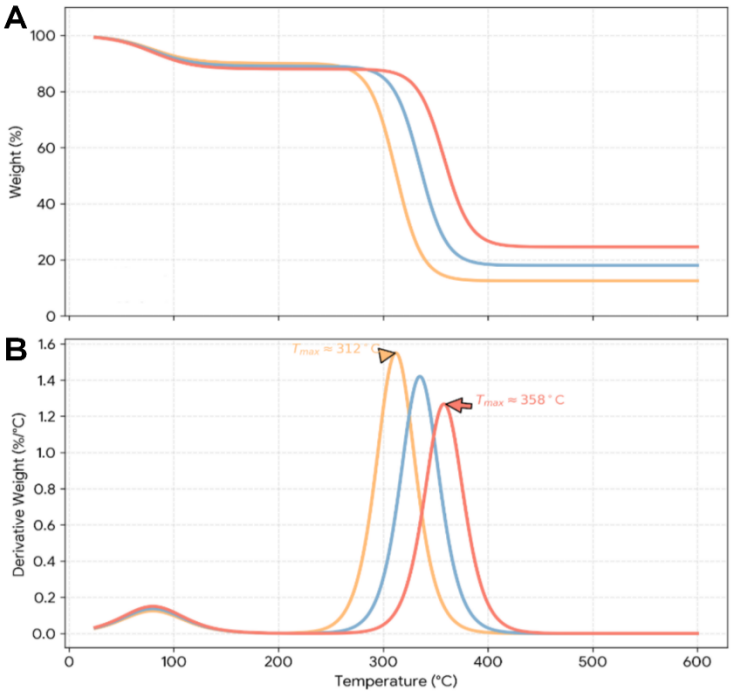

Figure 7. (A) TGA and (B) DTG curves of native corn starch (yellow curves), CS-CD-0 (blue curves), and CS-CD-3 (orange curves) recorded under nitrogen from 25 to 600 °C

10.57647/jnsc.2026.1602.08

At the extreme acidity of pH 1.2, used as a stringent test of stability, the ESR falls further to approximately ~780%. Here, most carboxylates are converted to neutral –COOH groups, electrostatic contributions are largely suppressed, and hydrogen bonding between polysaccharide chains and β-CD moieties becomes dominant, leading to partial collapse of the network. The monotonic reduction in swelling from pH 7.4 to 1.2 thus reflects a well-defined ionization-controlled behavior, confirming that the microgels function as classical anionic pH-sensitive gels. Fig. 9 further demonstrates that these pH-triggered volume transitions are not only significant but also highly reversible. Upon repeated alternation between pH 1.2 and 7.4, the ESR oscillates between low and high values with minimal loss of amplitude over successive cycles, indicating that the CS-CD-3 matrix can undergo multiple swelling–deswelling events without fragmentation or severe fatigue. This behavior is consistent with the presence of a dense, covalent poly(ether) network formed by epichlorohydrin crosslinking, which resists irreversible chain scission while allowing sufficient flexibility for large, reversible deformations [55]. The reversible 'on–off' swelling response is particularly important for drug delivery applications: in the neutral bloodstream the expanded, highly hydrated network and β-CD cavities can safely retain doxorubicin, whereas upon internalization into acidic endosomal/lysosomal compartments, protonation of doxorubicin can weaken β-CD host–guest association and increase the free-drug fraction, such that inclusion-complex dissociation becomes the dominant trigger for accelerated release even if the gel is less swollen than at pH 7.4.

3.6. Drug Loading and Encapsulation Efficiency

The data summarized in Fig. 10 demonstrate that incorporation of β-CD into the corn starch microgel network has a profound and systematic effect on the doxorubicin loading characteristics of the carriers. In the absence of β-CD (CS-CD-0), both the drug loading content and encapsulation efficiency are modest, with a DLC of 3.2% and an EE of 22.5%, indicating that simple physical entrapment within the crosslinked starch mesh is insufficient to achieve a therapeutically relevant payload. As the β-CD content is gradually increased, both parameters rise steeply, reaching DLC values above 11% and EE values close to or above 80% for the β-CD-rich formulations CS-CD-3 and CS-CD-4. This trend clearly supports the hypothesis that the dominant loading mechanism is not mere adsorption or diffusion into aqueous pores, but rather the formation of inclusion complexes between the hydrophobic anthracycline chromophore of DOX and the apolar cavity of β-CD units covalently anchored in the starch skeleton.

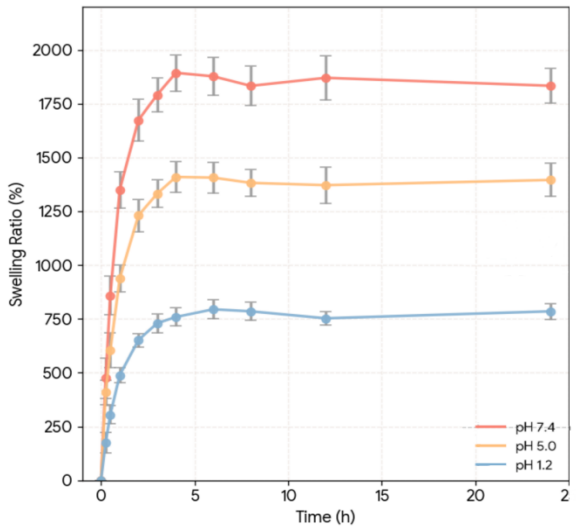

Figure 8. Time-dependent swelling behavior of CS-CD-3 composite microgels in buffer solutions of pH 1.2, 5.0 and 7.4 at 37 °C

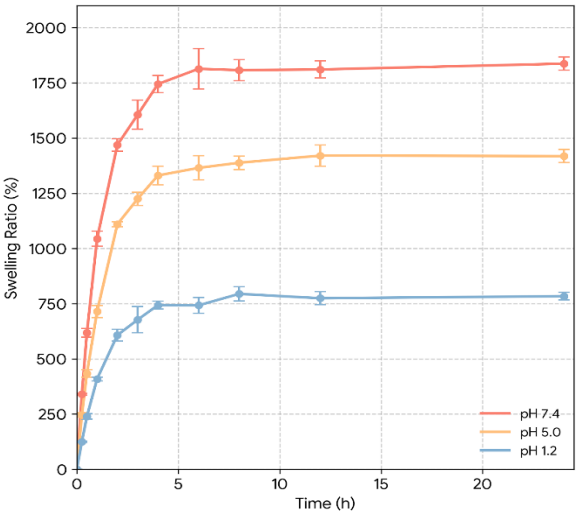

Figure 9. Reversible pH-responsive swelling–deswelling of CS-CD-3 composite microgels upon alternating transfer between acidic (pH 1.2) and physiological (pH 7.4) media at 37 °C

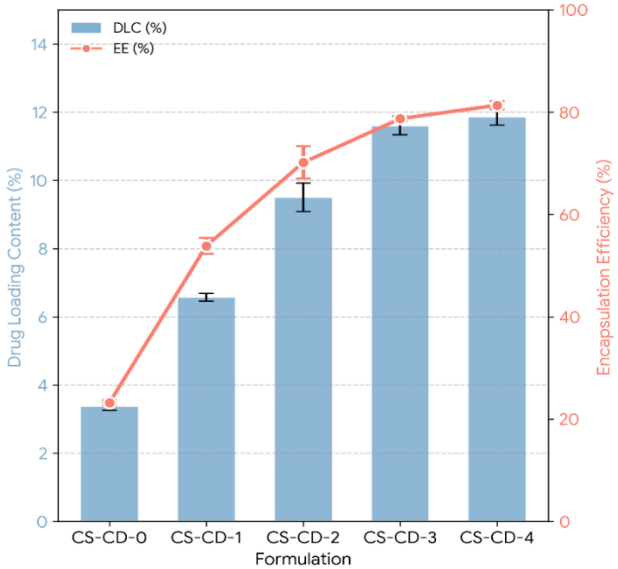

Figure 10. Drug loading content (DLC) and encapsulation efficiency (EE) of doxorubicin in CS-CD microgels with different β-CD contents (formulations CS-CD-0 to CS-CD-4). Data are expressed as mean ± SD (n = 3)

10.57647/jnsc.2026.1602.08

Interestingly, the incremental benefit of adding β-CD appears to level off as the formulation becomes highly CD-rich. Although CS-CD-4 exhibits slightly higher DLC and EE than CS-CD-3, the gain is relatively small compared with the pronounced increase observed when moving from starch-only CS-CD-0 to intermediate β-CD-containing formulations. When these results are interpreted in conjunction with the particle size, porosity, and release data, CS-CD-3 emerges as an optimal compromise: it offers very high encapsulation efficiency (78.4%) and drug loading (11.5%) while maintaining a hydrodynamic diameter in the mid-300 nm range and a well-developed mesoporous structure that favors diffusion-controlled release. In contrast, further increasing β-CD content may lead to larger, more aggregated particles and slightly reduced fractional release at physiological pH, which is undesirable for achieving a balance between high payload and controlled unloading. Fig. 11A provides supportive (non-standalone) spectroscopic evidence that the microenvironment of DOX changes after association with the CS–CD microgels. Free DOX shows a characteristic visible absorption band near 480 nm, which is routinely used for DOX quantification in drug-delivery studies. After loading into the CS–CD microgels, the DOX band exhibits a measurable shift and band-shape change, consistent with DOX experiencing a different local polarity and/or restricted conformational freedom within the carrier matrix. Importantly, because DOX optical absorption is intrinsically sensitive to solution conditions, we added a pH-dependent UV–vis reference dataset of free DOX measured under the same pH conditions used for release testing (PBS pH 7.4 and acetate buffer pH 5.0) (Fig. 11B). This control allows direct visual comparison of pH-driven spectral changes in the absence of carrier versus carrier-associated perturbations. The UV–vis results are therefore interpreted as complementary evidence, together with loading trends and the pH-triggered release behavior, rather than as definitive structural proof on their own.

3.7. In Vitro Drug Release Studies

The release profiles depicted in Figure 12 provide direct functional evidence that the CS-CD-3 microgels enable pH-modulated doxorubicin release. We emphasize that doxorubicin itself is intrinsically pH-sensitive (ionizable), and in this system the pH dependence arises primarily from pH-regulated DOX ionization and the consequent change in DOX–β-cyclodextrin association (bound versus free fraction), together with pH-dependent ionization/relaxation of the crosslinked polysaccharide network. At pH 7.4, which mimics the neutral conditions of blood plasma and healthy liver tissue, DOX is released in a slow and nearly linear fashion, with only about one quarter of the loaded drug (~24%) diffusing out of the carrier after 24 h and a still incomplete release even at extended times. This restrained liberation reflects not only diffusional hindrance within the crosslinked starch-based network, but also the strong host–guest partitioning of DOX into β-CD cavities, which reduces the fraction of 'free' DOX available to diffuse through the aqueous phase of the gel.

In other words, the relevant transport parameter is the effective diffusivity of DOX, which is strongly decreased when a substantial portion of the payload is reversibly bound as an inclusion complex within the microgel. At first glance, this behavior may appear inconsistent with the swelling data in Figure 8, where the equilibrium swelling ratio (ESR) is higher at pH 7.4 (~1850%) than at pH 5.0 (~1400%).

However, ESR-driven changes in mesh size are not necessarily proportional to release rate when specific binding dominates.

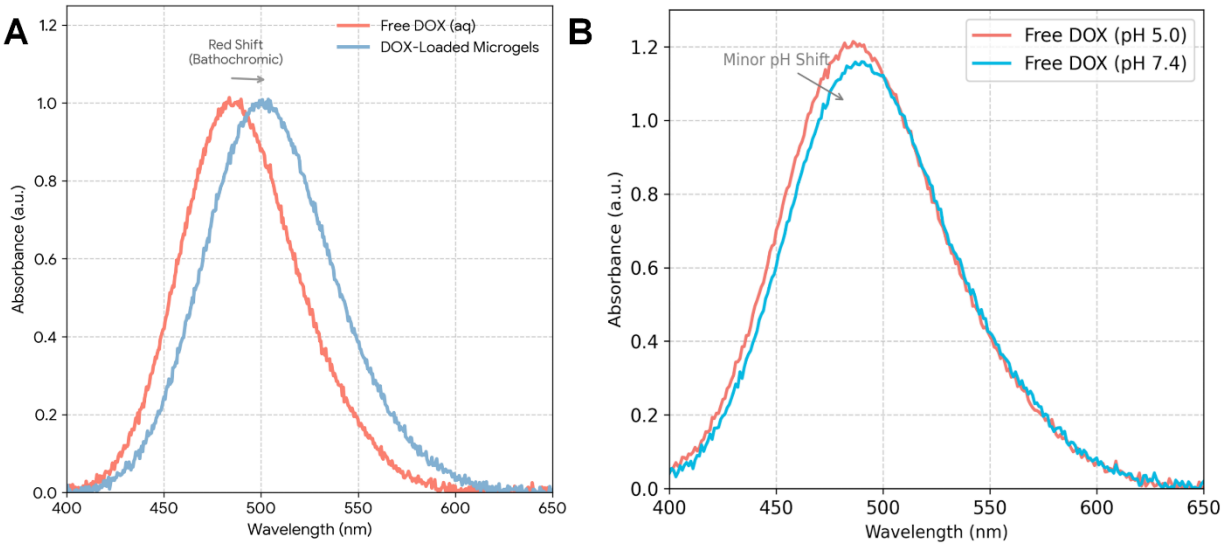

Figure 11. UV–vis absorption spectra related to doxorubicin (DOX). (A) Free DOX and DOX-associated CS–CD microgels under the stated measurement conditions. (B) pH-dependent UV–vis absorption spectra of free DOX measured in PBS (pH 7.4) and acetate buffer (pH 5.0) at the same DOX concentration

10.57647/jnsc.2026.1602.08

In the present system, the gel remains highly hydrated even at pH 5.0, and the relative difference in linear swelling between ESR ~1850% and ~1400% is modest compared with the chemical shift in DOX–β-CD association. Consequently, the pH response of the binding equilibrium (bound vs. free DOX) can outweigh the pH response of network expansion (pore size), producing an 'inverse' trend between swelling magnitude and release rate. In contrast, when the environmental pH is lowered to 5.0 the CS-CD-3 microgels exhibit a dramatically accelerated release, with approximately 72% of the encapsulated DOX liberated within the first 24 h. The dominant trigger is pH-dependent ionization of doxorubicin and the resulting weakening/dissociation of its β-CD inclusion complex.

At pH 5.0, the primary amino group of DOX is predominantly protonated (DOX–NH_3^+), which increases aqueous solubility and reduces the hydrophobic driving force for cyclodextrin inclusion, thereby shifting the equilibrium toward the uncomplexed ('free') state and promoting rapid outward diffusion. This pH-dependent decrease in host–guest affinity upon guest protonation is well precedented for cyclodextrin complexes and has been reported for DOX-containing cyclodextrin systems and related host–guest carriers, where acidic conditions accelerate DOX release primarily by disrupting inclusion/association rather than by maximizing gel swelling.

Simultaneously, partial protonation of ionizable groups within the starch/β-CD network reduces electrostatic repulsion and alters the osmotic balance, enabling local rearrangement of hydrated polymer chains and opening transient diffusion pathways. We therefore attribute the faster release at pH 5.0 to the combined effect of (i) a substantially increased free-DOX fraction due to inclusion-complex weakening and (ii) network relaxation that supports diffusion, whereas the high-swelling state at pH 7.4 primarily supports water uptake but still retains DOX through strong β-CD complexation and a tortuous poly(ether) network. The modest initial burst at early time points is attributed to loosely bound DOX near the particle surface, while the subsequent phase is governed by diffusion from the interior of the mesoporous microgel matrix.

Fig. 13 further elucidates the mechanisms governing DOX liberation by quantitatively fitting the release data at pH 5.0 to common kinetic models. The poor to moderate linearity observed for zero-order and first-order plots indicates that the release process cannot be described solely by a constant-rate erosion mechanism or by simple concentration-dependent desorption. Instead, the Higuchi plot (cumulative release versus square root of time) yields the highest correlation coefficient ($R^2 \approx 0.98$), indicating that diffusion through a hydrated, porous matrix is a dominant contributor over the investigated time scale. This conclusion is reinforced by the Korsmeyer–Peppas analysis, where the diffusional exponent $n \approx 0.62$ lies between 0.5 (Fickian diffusion) and 1.0 (case-II transport), placing the pH 5.0 dataset in the anomalous-transport range, i.e., a mixed contribution of diffusion and polymer relaxation/swelling in vitro.

Because these semi-empirical models are based on in vitro boundary conditions (buffer composition, sink conditions, and simplified geometry), the mechanistic assignment should be interpreted as an in vitro release descriptor rather than a direct statement of in vivo tumor-microenvironment transport.

In practical terms, this means that both DOX diffusion and polymer chain relaxation/swelling contribute significantly to the overall release behavior, which is consistent with the pH-dependent swelling–deswelling cycles previously observed for CS-CD-3 and with its soft, gel-like morphology.

3.8. Biocompatibility and Cytotoxicity

Fig. 14 first establishes that the blank, drug-free CS-CD-3 microgels are intrinsically safe toward both normal and malignant liver cells. After 24 h exposure to concentrations up to 500 μg/mL (polymer equivalent), L02 and HepG2 cells consistently maintained viability above 90%, with no evidence of dose-dependent decline. This result indicates that the crosslinked corn starch/β-CD/epichlorohydrin matrix does not elicit appreciable cytotoxicity on its own, and that any subsequent antiproliferative effects observed with the drug-loaded formulation can be attributed to the pharmacological action of DOX rather than to the carrier.

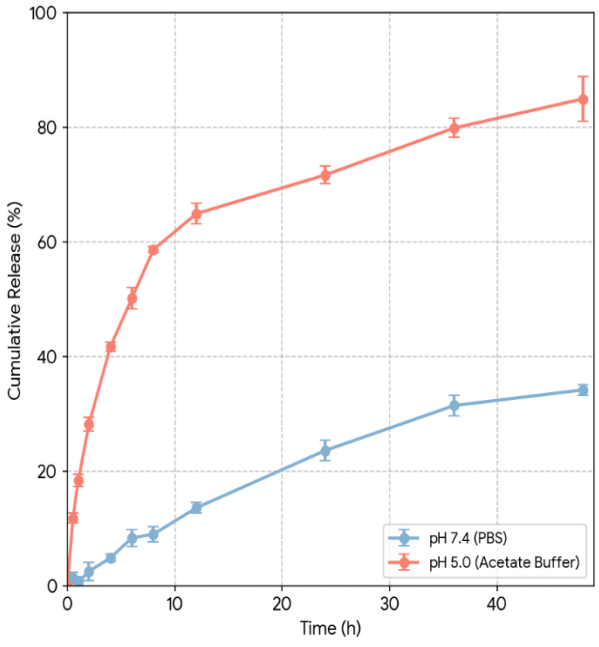

Figure 12. Cumulative in vitro release profiles of doxorubicin (DOX) from CS-CD-3 composite microgels in PBS (pH 7.4) and acetate buffer (pH 5.0) at 37 °C under sink conditions

10.57647/jnsc.2026.1602.08

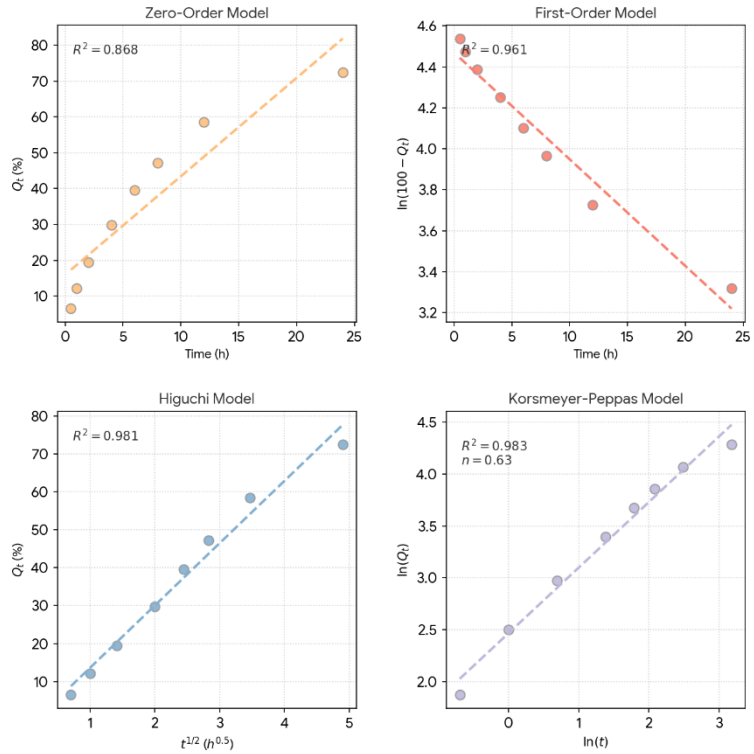

Figure 13. Kinetic modelling of DOX release from CS-CD-3 composite microgels at pH 5.0: linear fitting of the experimental data to zero-order, first-order, Higuchi, and Korsmeyer–Peppas models

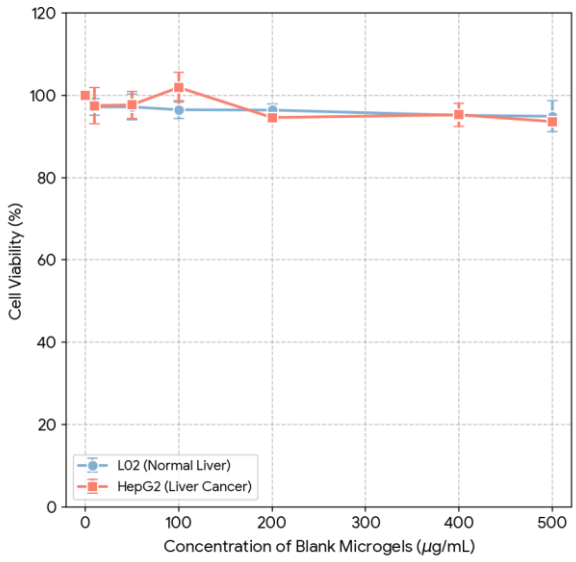

Figure 14. In vitro cytotoxicity of blank CS-CD-3 composite microgels toward L02 normal liver cells and HepG2 hepatocellular carcinoma cells after 24 h incubation, as determined by the MTT assay

The high tolerance of both cell types to blank microgels is consistent with the polysaccharide origin of the material and the absence of residual ECH, as inferred from spectroscopic and purification data, and it underpins the suitability of CS-CD-3 as a biocompatible platform for hepatocellular carcinoma therapy. Fig. 15 then examines how incorporation of DOX into CS-CD-3 alters the cytotoxic response of HepG2 cells compared with free drug. Both free DOX and DOX-CS-CD-3 produce a typical dose-dependent reduction in cell viability over 48 h, but the slope of the dose–response curve is steeper for the microgel formulation. At intermediate and high DOX-equivalent concentrations, HepG2 viability is consistently lower in the DOX-CS-CD-3 group than in the free DOX group, indicating that the same nominal drug dose is more effective at inhibiting cancer cell proliferation when delivered via the microgels.

This observation is quantified in Table 3, where the IC_{50} for HepG2 cells decreases from 2.15 ± 0.18 μg/mL for free DOX to 0.85 ± 0.12 μg/mL for DOX-CS-CD-3, corresponding to approximately a 2.5-fold increase in potency. Such an enhancement is consistent with the mechanistic design of the system: CS-CD-3 particles in the 300–400 nm size range are readily internalized by HepG2 cells through endocytic pathways, transporting a concentrated DOX payload into acidic endosomal/lysosomal compartments.

Under these conditions, protonation of DOX and partial relaxation of the pH-responsive starch/β-CD network promote rapid drug release, generating high local drug concentrations in close proximity to the nucleus and partially bypassing P-glycoprotein efflux pumps at the plasma membrane.

In contrast to the straightforward increase in potency toward HepG2 cells, the behavior in normal L02 cells reveals an equally important protective effect. While free DOX displays an IC50 of 4.50 ± 0.35 μg/mL in L02 cells, DOX-CS-CD-3 is significantly less toxic, with an IC50 of 8.20 ± 0.65 μg/mL. At equivalent DOX doses, viability of L02 cells is higher for the microgel formulation than for free drug, indicating that encapsulation into CS-CD-3

10.57647/jnsc.2026.1602.08

partially shields normal hepatocytes from DOX exposure. This protection can be explained by both extracellular and intracellular factors.

In the neutral extracellular environment (pH 7.4), DOX release from CS-CD-3 is strongly retarded, as demonstrated in the release studies, reducing the freely diffusible drug fraction available to normal cells. In addition, we expanded the uptake experiment to include L02 cells under identical exposure and imaging conditions as HepG2 (Section 2.7), and the resulting CLSM images (Figure 17D–F) show substantially weaker intracellular DOX fluorescence and fewer vesicular puncta in L02 cells after DOX-CS-CD-3 incubation, consistent with reduced internalization of the carrier in normal hepatocytes. These observations are consistent with prior reports that malignant cells often display higher nanoparticle uptake than normal hepatic cells due to differences in endocytic activity and trafficking.

Fig. 16 integrates these trends into a simple visual comparison, highlighting not only the absolute IC_{50} values but also the selectivity index (SI = IC_{50}, L02 / IC_{50}, HepG2). For free DOX, the SI of 2.09 indicates only modest preferential toxicity toward cancer cells; the therapeutic window is narrow, and significant collateral damage to normal liver tissue is expected at doses required for tumor control [56].

In stark contrast, DOX-CS-CD-3 achieves an SI of 9.64, representing more than a fourfold improvement in selectivity. This dramatic increase arises from the combination of decreased IC_{50} in HepG2 (enhanced efficacy) and increased IC_{50} in L02 (reduced off-target toxicity). From a pharmacological standpoint, such a shift in SI is highly significant: it suggests that, in vivo, lower systemic doses of DOX-CS-CD-3 could achieve equivalent or superior antitumor effects compared with free DOX, while simultaneously diminishing the risk of dose-limiting toxicities such as cardiomyopathy and hepatotoxicity [57].

3.9. Cellular Uptake and Intracellular Distribution

In Fig. 17, CLSM images clearly delineate distinct intracellular fluorescence patterns for free DOX and DOX-CS-CD-3 and, importantly, reveal cell-type differences between HepG2 and L02. After 2 h exposure to free DOX, HepG2 cells show diffuse red fluorescence throughout the cytoplasm and nucleus, reflecting the small, amphiphilic nature of the molecule and its ability to enter cells largely by passive diffusion.

In contrast, DOX-CS-CD-3 produces punctate perinuclear fluorescence in HepG2 cells at 2 h, consistent with vesicular localization typical of endocytic internalization. When the same experiment was performed in L02 cells using identical dosing and imaging settings (Fig. 17D–F), intracellular DOX fluorescence after DOX-CS-CD-3 exposure was markedly weaker and punctate vesicular signals were less frequent than in HepG2, indicating reduced microgel-associated uptake in normal hepatocytes.

These observations provide direct experimental support for the reduced L02 toxicity being attributable, in part, to lower internalization of the carrier in addition to retarded release at pH 7.4. While this rapid distribution enables DOX to access nuclear DNA, it is inherently non-selective and exposes the drug to efflux pumps at the plasma membrane, which contributes to multidrug resistance.

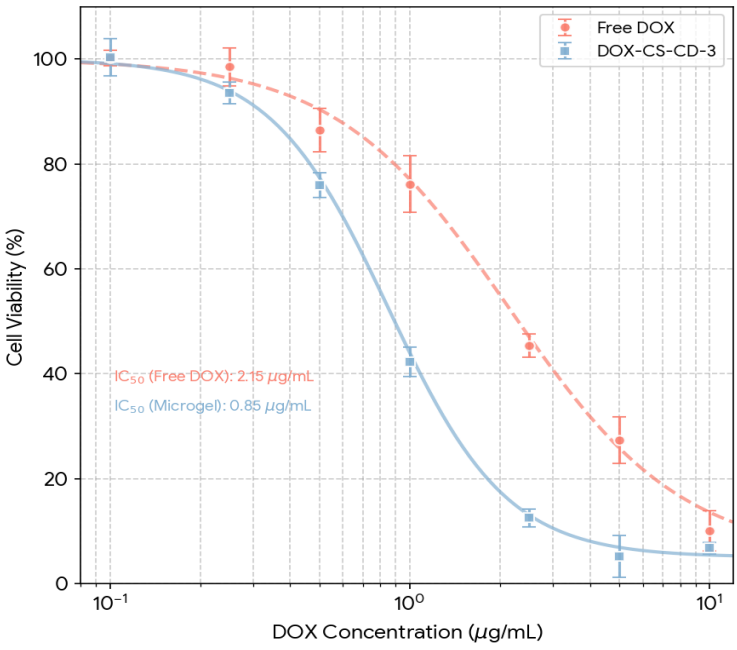

Figure 15. Dose-dependent cytotoxicity profiles of free doxorubicin (DOX) and DOX-loaded CS-CD-3 composite microgels (DOX-CS-CD-3) against HepG2 cells after 48 h incubation, evaluated by the MTT assay

10.57647/jnsc.2026.1602.08

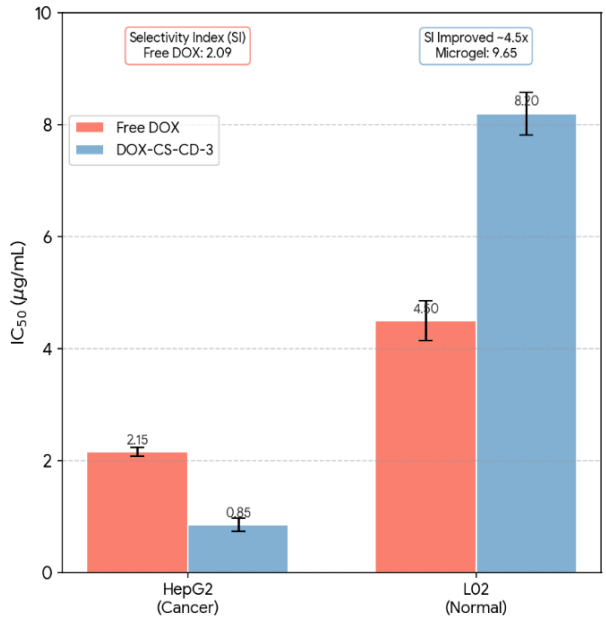

Figure 16. Comparison of IC_{50} values for free DOX and DOX-CS-CD-3 composite microgels in HepG2 hepatocellular carcinoma cells and L02 normal liver cells after 48 h incubation. IC_{50} values were obtained by nonlinear regression fitting of MTT viability curves and are expressed as mean ± SD (n = 3). For HepG2 cells, the IC_{50} decreased from 2.15 ± 0.18 μg/mL for free DOX to 0.85 ± 0.12 μg/mL for DOX-CS-CD-3, whereas for L02 cells it increased from 4.50 ± 0.35 μg/mL to 8.20 ± 0.65 μg/mL. The corresponding selectivity index (SI = IC_{50}, L02 / IC_{50}, HepG2) increased from 2.09 for free DOX to 9.64 for DOX-CS-CD-3, highlighting the markedly improved therapeutic window of the microgel formulation

Table 3. IC_{50} values (μg/mL) after 48h incubation

Treatment	HepG2 (Cancer)	L02 (Normal)	Selectivity Index (SI)[d]
Free DOX	2.15 ± 0.18	4.50 ± 0.35	2.09
DOX-CS-CD-3	0.85 ± 0.12	8.20 ± 0.65	9.64

Notes: [d]SI=IC_{50}(Normal)/IC_{50}(Cancer)

In contrast, cells treated with DOX-CS-CD-3 for the same duration exhibit discrete, punctate fluorescent spots localized mainly in the perinuclear cytoplasm, a pattern characteristic of vesicular structures such as endosomes and lysosomes [58].

This localization is consistent with endocytic internalization of the microgels, in line with their submicron size (~345 nm) and moderately negative surface charge, which favor clathrin- and caveolae-mediated uptake rather than passive diffusion.

The temporal evolution of the fluorescence pattern is the key readout for the carrier system. After 4 h incubation with DOX-CS-CD-3, HepG2 cells display intensified nuclear red fluorescence with reduced punctate cytoplasmic signal, indicating intracellular release followed by nuclear accumulation; this delayed nuclear enrichment explains why free DOX may appear brighter at earlier time points while the microgel formulation achieves effective intracellular delivery over time.

This shift indicates that the microgels, once internalized, are able to escape from endo/lysosomal compartments and release their DOX payload, which then diffuses into the nucleus where it can intercalate DNA and inhibit topoisomerase II.

The pH gradient within the endosomal–lysosomal pathway (pH ~5.0) is a key driver of this process: protonation of DOX reduces its affinity for the hydrophobic β-CD cavity and weakens host–guest inclusion, while partial relaxation of the anionic starch/CD network at acidic pH facilitates drug diffusion out of the gel matrix, as already evidenced by the accelerated release profile at pH 5.0. Together, these features effectively convert the CS-CD-3 microgels into intracellular depots that concentrate DOX in close proximity to the nucleus while shielding it from premature efflux during the uptake phase.

Fig. 18 translates these qualitative imaging observations into quantitative biological consequences. Annexin V-FITC/PI staining reveals that free DOX induces only a moderate level of apoptosis in HepG2 cells (~36% total apoptotic/necrotic population), despite its apparent nuclear accumulation at early time points.

This moderate effect is consistent with the relatively high IC_{50} value for free DOX and may reflect incomplete intracellular retention and active efflux by P-glycoprotein, which limits sustainable nuclear exposure. By contrast, DOX-CS-CD-3 raises the apoptotic/necrotic fraction to approximately 55%, representing a substantial enhancement in programmed cell death at the same nominal drug dose.

This finding dovetails with the ~2.5-fold decrease in IC_{50} for HepG2 cells and the pronounced improvement in selectivity index reported for the microgel formulation, demonstrating that more of the administered DOX is effectively converted into lethal nuclear insults when delivered via CS-CD-3 [59]. The higher apoptotic rate can be attributed to (i) greater intracellular accumulation of DOX due to efficient endocytosis and reduced susceptibility to P-gp efflux, (ii) pH-triggered release in endo/lysosomes resulting in local supersaturation of DOX, and (iii) sustained nuclear retention after microgel disassembly. Importantly, these pro-apoptotic effects are achieved without inherent toxicity of the carrier, as blank CS-CD-3 microgels maintain >90% viability in both HepG2 and L02 cells. Taken together, Figs. 17 and 18 provide compelling mechanistic evidence that the CS-CD-3 microgels not only increase DOX delivery to the nucleus of hepatocellular carcinoma cells but also translate this enhanced delivery into significantly stronger apoptotic signaling, thereby underpinning the improved therapeutic window of the DOX-CS-CD-3 system compared with free DOX.

10.57647/jnsc.2026.1602.08

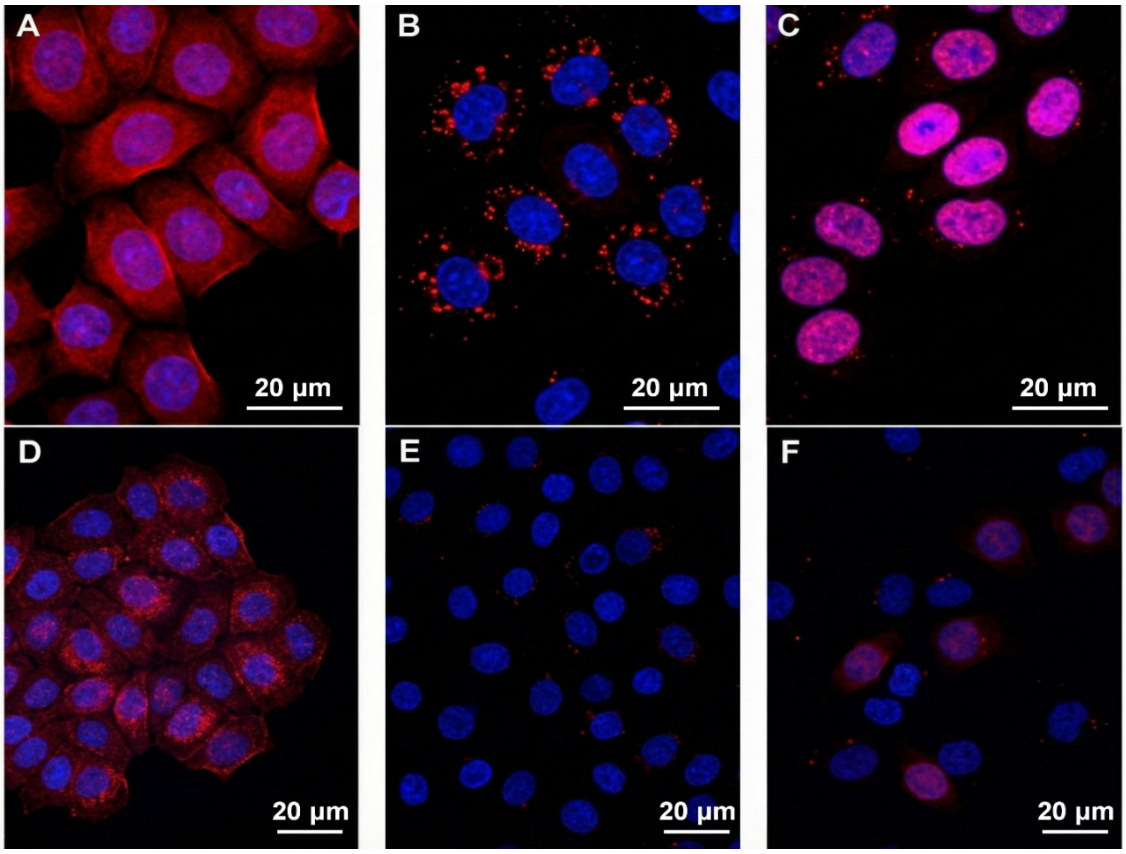

Figure 17. Confocal laser scanning microscopy (CLSM) images showing intracellular distribution of DOX fluorescence after treatment with free DOX or DOX-CS-CD-3 (DOX-equivalent concentration 5 μg/mL). (A–C) HepG2 cells: (A) free DOX for 2 h; (B) DOX-CS-CD-3 for 2 h; (C) DOX-CS-CD-3 for 4 h. (D–F) L02 cells under identical conditions: (D) free DOX for 2 h; (E) DOX-CS-CD-3 for 2 h; (F) DOX-CS-CD-3 for 4 h. Nuclei are stained with DAPI (blue). Representative images were acquired using the same CLSM settings across groups to enable qualitative comparison of intracellular fluorescence intensity

Figure 18. Flow cytometric analysis of HepG2 cell death after treatment with PBS (control), free DOX, or DOX-loaded CS-CD-3 microgels (DOX-CS-CD-3) using Annexin V-FITC/propidium iodide (PI) staining. Quadrant definitions were as follows: Q3 (Annexin V−/PI−), viable cells; Q4 (Annexin V+/PI−), early apoptosis; Q2 (Annexin V+/PI+), late apoptosis/secondary necrosis; Q1 (Annexin V−/PI+), necrotic cells. Percentages indicate the fraction of cells in each quadrant. Total apoptosis was calculated as Q2+Q4

4. Conclusion

In this work, we have developed and systematically characterized a family of nanostructured cyclodextrin-linked corn starch microgels as a bio-based platform for pH-responsive doxorubicin delivery to hepatocellular carcinoma. By tailoring the β-cyclodextrin content and epichlorohydrin crosslinking density, we obtained colloidally stable nanoscale microgels with negative surface charge and well-defined internal nanostructures. Comprehensive physicochemical analyses (FTIR, XRD, TGA/DTG, DSC, SEM, and DLS) together with nitrogen sorption measurements confirmed the formation of mesoporous polymer networks, as illustrated by the CS-CD-3 formulation which exhibited an increased BET specific surface area and nanometer-scale pore sizes. These nanostructured polymer networks provided abundant host–guest interaction sites and diffusion pathways for doxorubicin, enabling high encapsulation efficiency (up to 78.4%) and controlled drug loading

10.57647/jnsc.2026.1602.08

within the microgels. From a functional perspective, the microgels behaved as efficient tumor-microenvironment-responsive nanocarriers. In vitro release experiments demonstrated markedly pH-dependent release profiles, with limited doxorubicin leakage at physiological pH 7.4 and substantially accelerated release under mildly acidic conditions mimicking the endo-lysosomal and tumor milieu. Blank microgels showed high cytocompatibility toward both HepG2 and L02 cells, whereas doxorubicin-loaded CS-CD-3 microgels enhanced anticancer efficacy in HepG2 cells and simultaneously improved safety in normal hepatocytes, resulting in a pronounced increase in therapeutic selectivity (selectivity index up to 9.64). Confocal microscopy and flow cytometry further corroborated the nanoscopic mode of action, revealing efficient endocytic uptake, intracellular trafficking, and apoptosis induction. Overall, this study establishes cyclodextrin–starch microgels as a promising nanostructured, mesoporous polysaccharide nanoplatform that bridges green nanochemistry with targeted cancer nanomedicine. Future work will focus on fine-tuning the nano-architecture and surface chemistry, co-loading multi-drug combinations, and performing in vivo pharmacokinetics and biodistribution studies in orthotopic HCC models to fully exploit the potential of this nanogel system. While the in vitro kinetic modeling provides a useful mechanistic descriptor of release under controlled buffer conditions, confirmation of transport behavior under physiological complexity requires in vivo pharmacokinetics, biodistribution, and efficacy studies.

Acknowledgements

This work has been supported by Medical Science Research Project of Hebei (20230117).

Author Contributions

S.W. conceived and designed the study, developed the methodology, carried out the experimental investigation, performed formal data analysis, curated the data, and wrote the original draft of the manuscript. T.P. contributed to methodology development, assisted with formal analysis, and participated in manuscript review and editing. J.Z. and H.G. conducted experimental investigations and contributed to data acquisition and visualization. W.Y. provided overall supervision, conceptual guidance, and project administration, contributed to data interpretation, reviewed and edited the manuscript, and was responsible for funding acquisition. All authors have read and agreed to the published version of the manuscript.

Availability of data and materials

The data that support the findings of this study are available from the corresponding author upon reasonable request.

Conflict of interests

The authors declare no conflicts of interest to report regarding the present study.

Reference

[1] Chan, S.L., Sun, H.-C., Xu, Y., Zeng, H., El-Serag, H.B., Lee, J.M., Schwartz, M.E., Finn, R.S., Seong, J., Wang, X.W., Paradis, V., Abou-Alfa, G.K., Rimassa, L., Kao, J.-H., Zhang, B.-H., Llovet, J.M., Bruix, J., Yip, T.C.-F., Wong, V.W.-S., Wong, G.L.-H., Chan, L.L., Liu, M.-Q., Gao, Q., Shen, F., Kelley, R.K., Cheng, A.-L., Kurosaki, M., Toyoda, H., Chen, W.-X., Murakami, T., Liang, P., Zucman-Rossi, J., Minami, Y., Miyayama, S., Wang, K., Man, K., Hasegawa, K., Li, Q., Tsuchiya, K., Xu, L., Chew, V., Chow, P., Hoshida, Y., Lujambio, A., Ng, I.O.-L., Sakamoto, M., Park, Y.N., Yau, T., Kudo, M., Fan, J., Zhou, J. The Lancet Commission on addressing the global hepatocellular carcinoma burden: comprehensive strategies from prevention to treatment. *Lancet* **406**, 731–778 (2025).

[2] Pulumati, A., Pulumati, A., Dwarakanath, B.S., Verma, A., Papineni, R.V.L. Technological advancements in cancer diagnostics: improvements and limitations. *Cancer Rep.* **6**, e1764 (2023).

[3] Anand, U., Dey, A., Chandel, A.K.S., Sanyal, R., Mishra, A., Pandey, D.K., De Falco, V., Upadhyay, A., Kandimalla, R., Chaudhary, A., Dhanjal, J.K., Dewanjee, S., Vallamkondu, J., Pérez de la Lastra, J.M. Cancer chemotherapy and beyond: current status, drug candidates, associated risks and progress in targeted therapeutics. *Genes Dis.* **10**, 1367–1401 (2022).

[4] Sinha, S.J., Kumar, B., Prasad, C.P., Chauhan, S.S., Kumar, M. Emerging research and future directions on doxorubicin: a snapshot. *Asian Pac. J. Cancer Prev.* **26**, 5–15 (2025).

[5] Sritharan, S., Sivalingam, N. A comprehensive review on time-tested anticancer drug doxorubicin. *Life Sci.* **278**, 119527 (2021).

[6] Lim, J.X., Yong, Y.K., Dewi, F.R.P., Chan, S.Y., Lim, V. Nanoscale strategies: doxorubicin resistance challenges and enhancing cancer therapy with advanced nanotechnological approaches. *Drug Deliv. Transl. Res.* **15**, 3835–3863 (2025).

[7] Kumbhar, D.C.J.R. Stimuli-responsive (smart) drug delivery systems: an in-depth review. (2025).

[8] Scheffold, F. Pathways and challenges towards a complete characterization of microgels. *Nat. Commun.* **11**, 4315 (2020).

[9] Aparna, T.N., Kumar, R., Ali, S.R., Patel, D.J., Julekha, K., Begum, T., Bala, J., Kumar, P. Silica nanoparticles: a promising vehicle for anti-cancer drugs delivery. *AAPS PharmSciTech* **26**, 33 (2025).

[10] Baumann, F., Paul, T., Wassersleben, S., Regenthal, R., Enke, D., Aigner, A. Characterization of drug release from mesoporous SiO_2-based membranes with variable pore structure and geometry. *Pharmaceutics* **14**, 1184 (2022).

[11] Benalaya, I., Alves, G., Lopes, J., Silva, L.R. A review of natural polysaccharides: sources, characteristics, properties, food, and pharmaceutical applications. *Int. J. Mol. Sci.* **25**, 1322 (2024).

[12] Jabeen, N., Atif, M. Polysaccharides based biopolymers for biomedical applications: a review. *Polym. Adv. Technol.* **35**, e6203 (2024).

[13] Behrooznia, Z., Nourmohammadi, J. Polysaccharide-based materials as an eco-friendly alternative in biomedical, environmental, and food packaging. *Giant* **19**, 100301 (2024).

[14] Yu, J.-K., Moon, Y.-S. Corn starch: quality and quantity improvement for industrial uses. *Plants* **11**, 92 (2022).

[15] Amaraweera, S.M., Gunathilake, C., Gunawardene, O.H.P., Fernando, N.M.L., Wanninayaka, D.B., Dassanayake, R.S., Rajapaksha, S.M., Manamperi, A., Fernando, C.A.N., Kulatunga, A.K., Manipura, A. Development of starch-based materials using current modification techniques and their applications: a review. *Molecules* **26**, 6880 (2021).

[16] Li, Y., Zhang, F., Wang, B., Liu, J., Wang, Y., Shi, Z., Du, L., Wang, K., Zhang, W., Wang, Z., Dou, L. Synergistic epichlorohydrin-crosslinked carboxymethyl xylan for enhanced thermal stability and filtration control in water-based drilling fluids. *Gels* **11**, 666 (2025).

[17] Chen, L., Zhang, D., Wei, L.-F., Zhu, W.-J., Yan, X.-Q., Zhou, R., Din, Z., Ding, W.-P., Ma, T.-Z., Cai, J. Structural and mechanistic insights into starch microgel/anthocyanin complex assembly and controlled release performance. *Int. J. Biol. Macromol.* **213**, 718–727 (2022).

[18] Xu, W., Li, X., Wang, L., Li, S., Chu, S., Wang, J., Li, Y., Hou, J., Luo, Q., Liu, J. Design of cyclodextrin-based functional systems for biomedical applications. *Front. Chem.* **9** (2021).

[19] Zhao, R., Tang, B., Xu, Z., Fang, G. β-Cyclodextrin-based polyelectrolyte complexes for drug delivery. *Coord. Chem. Rev.* **534**, 216581 (2025).

[20] Nanda, D., Behera, D., Pattnaik, S.S., Behera, A.K. Advances in natural polymer-based hydrogels: synthesis, applications, and future directions in biomedical and environmental fields. *Discov. Polym.* **2**, 6 (2025).

[21] Nanta, P., Kasemwong, K., Grisdanurak, N. Production and characterization of starch microspheres using supercritical carbon dioxide assisted spray drying. *Int. J. Biol. Macromol.* **305**, 141197 (2025).

[22] Vagena, I.-A., Malapani, C., Gatou, M.-A., Lagopati, N., Pavlatou, E.A. Enhancement of EPR effect for passive tumor targeting: current status and future perspectives. *Appl. Sci.* **15**, 3189 (2025).

[23] Hosonuma, M., Yoshimura, K. Association between pH regulation of the tumor microenvironment and immunological state. *Front. Oncol.* **13**, 1175563 (2023).

[24] Obadi, M., Qi, Y., Xu, B. High-amylose maize starch: structure, properties, modifications and industrial applications. *Carbohydr. Polym.* **299**, 120185 (2023).

[25] Madrid, F., Rubio-Bellido, M., Morillo, E. Extraction of nonylphenol, pyrene and phenanthrene from sewage sludge and composted biosolids by cyclodextrins and rhamnolipids. *Sci. Total Environ.* **715**, 136986 (2020).

[26] Krishnan, K.K., Thomas, A.M., Sindhu, K.S., Anilkumar, G. Recent advances and perspectives in the manganese-catalysed epoxidation reactions. *Tetrahedron* **72**, 1–16 (2016).

[27] Mehryab, F., Ebrahimi, M., Baharvand, H., Haeri, A., Shekari, F. Extracellular vesicle-based formulation of doxorubicin: drug loading optimization, characterization, and cytotoxicity evaluation in tumor spheroids. *Pharm. Dev. Technol.* **29**, 727–737 (2024).

[28] Lv, Y., He, H., Qi, J., Lu, Y., Zhao, W., Dong, X., Wu, W. Visual validation of the measurement of entrapment efficiency of drug nanocarriers. *Int. J. Pharm.* **547**, 395–403 (2018).

[29] Oh, Y.J., Hong, J. Application of the MTT-based colorimetric method for evaluating bacterial growth using different solvent systems. *LWT* **153**, 112565 (2022).

[30] Jonkman, J., Brown, C.M., Wright, G.D., Anderson, K.I., North, A.J. Tutorial: guidance for quantitative confocal microscopy. *Nat. Protoc.* **15**, 1585–1611 (2020).

[31] Wu, S., Hatahet, T., Bona, B.L., Lodigiani, G., Zhang, M., Bombelli, F.B., Al-Jamal, W.T. Incorporating Span 80 surfactant into lipid nanocapsules improves their biocompatibility and cellular uptake in B16F10 melanoma cells. *Int. J. Pharm.* **672**, 125358 (2025).

[32] Salleh, K.M., Zakaria, S., Sajab, M.S., Gan, S., Chia, C.H., Jaafar, S.N.S., Amran, U.A. Chemically crosslinked hydrogel and its driving force towards superabsorbent behaviour. *Int. J. Biol. Macromol.* **118**, 1422–1430 (2018).

[33] Nicu, R., Lisa, G., Darie-Nita, R.N., Avadanei, M.I., Bargan, A., Rusu, D., Ciolacu, D.E. Tailoring the structure and physico-chemical features of cellulose-based hydrogels using multi-epoxy crosslinking agents. *Gels* **10**, 523 (2024).

[34] Zeng, Y., Zhao, M., Zeng, H., Jiang, Q., Ming, F., Xi, K., Wang, Z., Liang, H. Recent progress in advanced catalysts for electrocatalytic hydrogenation of organics in aqueous conditions. *eScience* **3**, 100156 (2023).

[35] Vogel, R., Pal, A.K., Jambhrunkar, S., Patel, P., Thakur, S.S., Reátegui, E., Parekh, H.S., Saá, P., Stassinopoulos, A., Broom, M.F. High-resolution single particle zeta potential characterisation of biological nanoparticles using tunable resistive pulse sensing. *Sci. Rep.* **7**, 17479 (2017).

[36] Greenfield, N.J. Using circular dichroism spectra to estimate protein secondary structure. *Nat. Protoc.* **1**, 2876–2890 (2006).

[37] Park, S.-H. Cd content dependence of in-plane optical polarization in anisotropically strained c-plane CdZnO/ZnO quantum wells. *Physica B* **596**, 412393 (2020).

[38] Lim, S.H., Wong, T.W., Tay, W.X. Overcoming colloidal nanoparticle aggregation in biological milieu for cancer therapeutic delivery: perspectives of materials and particle design. *Adv. Colloid Interface Sci.* **325**, 103094 (2024).

[39] Kypr, J., Kejnovská, I., Renčiuk, D., Vorlíčková, M. Circular dichroism and conformational polymorphism of DNA. *Nucleic Acids Res.* **37**, 1713–1725 (2009).

[40] Wang, L., Chen, S., Li, C., Gu, Z., Kong, H., Ban, X., Li, Z. Enhancement of β-cyclodextrin production using a glycogen debranching enzyme from *Saccharolobus solfataricus* STB09. *J. Agric. Food Chem.* **72**, 6491–6499 (2024).

[41] Yang, X., Yokokura, S., Nagahama, T., Yamaguchi, M., Shimada, T. Molecular dynamics simulation of poly(ether ether ketone) polymer to analyze intermolecular ordering by low wavenumber Raman spectroscopy and X-ray diffraction. *Polymers* **14**, 5406 (2022).

[42] Li, Z., Pu, L., Hou, D., Yan, J., Zeng, Q., Chen, Y. A macrocycle-assisted platform approach to protein cross-linking via chemically inactive residues. *Nano Lett.* **25**, 3489–3496 (2025).

[43] Krishnaswamy, S. IR spectrum and characteristic absorption bands. (n.d.).

[44] Zhou, J., Zhang, Z., Li, X., Yin, J., Zhou, J., Wu, M. A novel fingerprint recognition strategy driven by convolutional autoencoders and attention mechanisms. in: *Proc. 4th Int. Conf. Artificial Intelligence, Robotics, and Communication*, 893–900 (2024).

[45] Glover, J.D., Sudderick, Z.R., Shih, B.B.-J., Batho-Samblas, C., Charlton, L., Krause, A.L., Anderson, C., Riddell, J., Balic, A., Li, J., Klika, V., Woolley, T.E., Gaffney, E.A., Corsinotti, A.,

Anderson, R.A., Johnston, L.J., Brown, S.J., Wang, S., Chen, Y., Crichton, M.L., Headon, D.J. The developmental basis of fingerprint pattern formation and variation. *Cell* **186**, 940–956.e20 (2023).

[46] Wang, H., Zhao, P., Ma, R., Jia, J., Fu, Q. Drug–drug co-amorphous systems: an emerging formulation strategy for poorly water-soluble drugs. *Drug Discov. Today* **29**, 103883 (2024).

[47] Datta, K., van Laar, S.C.W., Taddei, M., Hidalgo, J., Kodalle, T., Aalbers, G.J.W., Lai, B., Li, R., Tamura, N., Frencken, J.T.W., Quiroz Monnens, S.V., Westbrook, R.J.E., Graham, D.J., Sutter-Fella, C.M., Correa-Baena, J.-P., Ginger, D.S., Wienk, M.M., Janssen, R.A.J. Local halide heterogeneity drives surface wrinkling in mixed-halide wide-bandgap perovskites. *Nat. Commun.* **16**, 1967 (2025).

[48] Rivas-Barbosa, R., Camerin, F., Vialetto, J., Ramakrishna, S.N., Isa, L., Zaccarelli, E. Comparing the structure of microgels at liquid–liquid and solid–liquid interfaces. *Langmuir* **41**, 16674–16684 (2025).

[49] Gordillo-Galeano, A., Mora-Huertas, C.E. Hydrodynamic diameter and zeta potential of nanostructured lipid carriers: emphasizing some parameters for correct measurements. *Colloids Surf. A* **620**, 126610 (2021).

[50] Chen, K., Zhang, T., Chen, X., He, Y., Liang, X. Model construction of micro-pores in shale: a case study of Silurian Longmaxi Formation shale in Dianqianbei area, SW China. *Pet. Explor. Dev.* **45**, 412–421 (2018).

[51] Chai, L., Wang, P., Liu, X., Sun, Y., Li, X., Pan, J. Accurately control the micropore/mesopore ratio to construct a new hierarchical porous carbon with ultrahigh capacitance and rate performance. *J. Power Sources* **532**, 231324 (2022).

[52] Xu, B., Li, S., Shi, R., Liu, H. Multifunctional mesoporous silica nanoparticles for biomedical applications. *Signal Transduct. Target. Ther.* **8**, 435 (2023).

[53] He, Y., Zheng, Y., Liu, C., Zhang, H., Shen, J. Citric acid cross-linked β-cyclodextrins: a review of preparation and environmental/biomedical application. *Carbohydr. Polym.* **323**, 121438 (2024).

[54] Sichina, W.J. Characterization of polymers using TGA. (n.d.).

[55] Wu, Z., Chu, C., Jin, Y., Yang, L., Qian, B., Wang, Y., Wang, Y., Wu, J., Jia, Y., Zhang, W., You, Z. Dynamic cross-linked topological network reconciles the longstanding contradictory properties of polymers. *Sci. Adv.* **11**, eadt0825 (2025).

[56] Mal, A., Prabhuraj, R.S., Malhotra, R., Valvi, S.K., Ingle, A., Srivastava, R., De, A., Bandyopadhyaya, R. pH-responsive sustained delivery of doxorubicin using aminated and PEGylated mesoporous silica nanoparticles leads to enhanced antitumor efficacy in pre-clinical orthotopic breast cancer model. *J. Drug Deliv. Sci. Technol.* **77**, 103800 (2022).

[57] Tsuchitani, T., Kato, M., Tomaru, A., Aoki, Y., Sugiyama, Y. Trends of in vitro pharmacological potency and in vivo pharmacokinetics parameters of modern drugs: can the therapeutic/subtherapeutic dose be estimated from in vitro Ki and pharmacokinetic parameters? *Clin. Transl. Sci.* **17**, e70034 (2024).

[58] Kciuk, M., Gielecińska, A., Mujwar, S., Kołat, D., Kałuzińska-Kołat, Ż., Celik, I., Kontek, R. Doxorubicin—an agent with multiple mechanisms of anticancer activity. *Cells* **12**, 659 (2023).

[59] Zhang, M., Zhang, G., Meng, X., Wang, X., Xie, J., Wang, S., Wang, B., Wang, J., Liu, S., Huang, Q., Yang, X., Li, J., Wang, H. Reduction of the oxidative damage to H_2O_2-induced HepG2 cells via the Nrf2 signalling pathway by plant flavonoids quercetin and hyperoside. *Food Sci. Hum. Wellness* **13**, 1864–1876 (2024).